

Haverford College

Haverford Scholarship

Faculty Publications

Astronomy

2020

Atacama Cosmology Telescope: Dusty Star-forming Galaxies and Active Galactic Nuclei in the Equatorial Survey

Megan B. Gralla

Tobias A. Marriage

Graeme Addison

Andrew J. Baker

Bruce Partridge

Follow this and additional works at: https://scholarship.haverford.edu/astronomy_facpubs



Atacama Cosmology Telescope: Dusty Star-forming Galaxies and Active Galactic Nuclei in the Equatorial Survey

Megan B. Gralla¹ , Tobias A. Marriage² , Graeme Addison² , Andrew J. Baker³ , J. Richard Bond⁴, Devin Crichton⁵ , Rahul Datta², Mark J. Devlin⁶, Joanna Dunkley^{7,8}, Rolando Dünner⁹, Joseph Fowler^{7,10}, Patricio A. Gallardo¹¹, Kirsten Hall², Mark Halpern¹² , Matthew Hasselfield¹³, Matt Hilton⁵ , Adam D. Hincks⁴, Kevin M. Huffenberger¹⁴ , John P. Hughes³ , Arthur Kosowsky¹⁵, Carlos H. López-Caraballo^{9,16}, Thibaut Louis^{17,18}, Danica Marsden^{6,19}, Kavilan Moodley⁵, Michael D. Niemack¹¹, Lyman A. Page⁷ , Bruce Partridge²⁰, Jesus Rivera³ , Jonathan L. Sievers⁵, Suzanne Staggs⁷ , Ting Su² , Daniel Swetz^{6,10}, and Edward J. Wollack²¹

¹ Department of Astronomy/Steward Observatory, University of Arizona, 933 N. Cherry Ave., Tucson, AZ 85721, USA

² Department of Physics and Astronomy, Johns Hopkins University, 3400 N. Charles St., Baltimore, MD 21218, USA

³ Department of Physics and Astronomy, Rutgers University, 136 Frelinghuysen Rd., Piscataway, NJ 08854-8019, USA

⁴ Canadian Institute for Theoretical Astrophysics, University of Toronto, 60 St. George St., Toronto, ON M5S 3H8, Canada

⁵ Astrophysics & Cosmology Research Unit, School of Mathematics, Statistics & Computer Science, University of KwaZulu-Natal, Westville Campus, Durban 4041, South Africa

⁶ Department of Physics and Astronomy, University of Pennsylvania, 209 South 33rd St., Philadelphia, PA 19104, USA

⁷ Joseph Henry Laboratories of Physics, Jadwin Hall, Princeton University, Princeton, NJ 08544, USA

⁸ Department of Astrophysical Sciences, Peyton Hall, Princeton University, Princeton, NJ 08544, USA

⁹ Instituto de Astrofísica and Centro de Astro-Ingeniería, Facultad de Física, Pontificia Universidad Católica de Chile, Av. Vicuña Mackenna 4860, 7820436 Macul, Santiago, Chile

¹⁰ NIST Quantum Sensors Group, Boulder, CO 80305, USA

¹¹ Department of Physics, Cornell University, Ithaca, NY 14853, USA

¹² Department of Physics and Astronomy, University of British Columbia, Vancouver, BC V6T 1Z4, Canada

¹³ Department of Astronomy and Astrophysics, The Pennsylvania State University, University Park, PA 16802, USA

¹⁴ Department of Physics, Florida State University, Tallahassee, FL 32306, USA

¹⁵ Department of Physics and Astronomy, University of Pittsburgh, Pittsburgh, PA 15260, USA

¹⁶ Departamento de Matemáticas, Universidad de La Serena, Av. Juan Cisternas 1200, La Serena, Chile

¹⁷ Institut d'Astrophysique de Paris, F-75014 Paris, France

¹⁸ LAL, Univ. Paris-Sud, CNRS/IN2P3, Université Paris-Saclay, Orsay, France

¹⁹ D-Wave Systems, 3033 Beta Avenue, Burnaby, BC V5G 4M9, Canada

²⁰ Department of Physics and Astronomy, Haverford College, Haverford, PA 19041, USA

²¹ NASA/Goddard Space Flight Center, Greenbelt, MD 20771, USA

Received 2019 May 1; revised 2019 December 1; accepted 2019 December 2; published 2020 April 21

Abstract

We present a catalog of 510 radio-loud active galactic nuclei (AGNs, primarily blazars) and 287 dusty star-forming galaxies (DSFGs) detected by the Atacama Cosmology Telescope at $>5\sigma$ significance in frequency bands centered on 148 GHz (2 mm), 218 GHz (1.4 mm), and 277 GHz (1.1 mm), from a 480 deg² strip centered at R.A. 00^h on the celestial equator with additional 360 deg² shallower auxiliary fields at other longitudes. The combination of the deepest available 218 GHz wide-field imaging, our 277 GHz data, and multiband filtering results in the most sensitive wide-field millimeter-wave DSFG selection to date, with rms noise level referenced to 218 GHz reaching below 2 mJy. We have developed new techniques to remove Galactic contamination (including evidence for CO (2–1) line emission) from the extragalactic catalog, yielding a catalog of 321 Galactic sources in addition to the extragalactic catalog. We employ a new flux debiasing method that accounts for the heterogeneous sample selection in the presence of Galactic cuts. We present the spectral properties and source counts of the AGNs and DSFGs. The DSFG spectra depart from the Rayleigh–Jeans regime of an optically thin modified blackbody between 218 and 277 GHz, consistent with optically thick emission or an additional cold dust component. For AGNs with 148 and 218 GHz flux density >50 mJy, we estimate the interyear rms fractional deviation in flux density due to source variability to be 40% with a 0.98 interband correlation coefficient. We provide source counts for AGNs in the range of 8–2870 mJy and for DSFGs in the range of 8–90 mJy. Our DSFG counts probe both the brighter, lensed population and the fainter, unlensed population. At 277 GHz we report the first measurements of source counts at these flux densities, finding an excess above most model count predictions. Finally, we present 30 of the brightest DSFGs that were selected for multifrequency study as candidate high- z lensed systems.

Unified Astronomy Thesaurus concepts: [Radio source catalogs \(1356\)](#); [Radio sources \(1358\)](#); [Radio source counts \(1357\)](#); [Extragalactic radio sources \(508\)](#); [Galactic radio sources \(571\)](#); [Cosmic microwave background radiation \(322\)](#); [Blazars \(164\)](#); [Submillimeter astronomy \(1647\)](#)

Supporting material: figure set

1. Introduction

Wide-field millimeter-wave surveys open a unique window on the extragalactic universe beyond their traditional

association with the primordial cosmic microwave background (CMB). In particular, galaxies are detected in these surveys through their millimeter-wave emission. Strong extragalactic

sources of millimeter emission fall into two categories. The first source category is characterized by self-absorbing synchrotron radiation extending from radio to millimeter wavelengths. In these sources, jets from active galactic nuclei (AGNs) impart relativistic velocities to electrons that in turn generate synchrotron radiation in the galaxy’s magnetic field. Self-absorption of synchrotron radiation is observed when the optically thick emission core of the AGN is within the observer’s line of sight. These sources are categorized observationally as blazars, BL Lacertae objects, or flat-spectrum radio quasars (FSRQs).²² Measurements of their synchrotron spectra provide a unique perspective on AGN jets (e.g., Blandford & Königl 1979; Toffolatti et al. 1998; de Zotti et al. 2005; Tucci et al. 2011). The second source category is characterized by thermal radiation from dust extending from millimeter to far-infrared wavelengths. The dust is heated by UV and optical emission, notably from massive young stars in these dusty star-forming galaxies (DSFGs). Since the first studies of DSFGs as submillimeter galaxies at 850 μm (SMGs; e.g., Smail et al. 1997; Barger et al. 1998; Hughes et al. 1998), we have learned that the most prodigious star formation in the universe generates and is enshrouded by significant dust, making DSFGs important in the history of cosmic star formation (e.g., Lilly et al. 1996; Madau et al. 1996; Blain et al. 2002; Chapman et al. 2005; Le Floch et al. 2005; Pérez-González et al. 2005; Hopkins & Beacom 2006; Daddi et al. 2007; Elbaz et al. 2007; Casey et al. 2014; Madau & Dickinson 2014).

Current state-of-the-art wide-field ($>100 \text{ deg}^2$) millimeter-wave source surveys have been conducted by three observatories: the Atacama Cosmology Telescope (ACT; Marriage et al. 2011; Marsden et al. 2014), the *Planck* Satellite (Planck Collaboration et al. 2011c, 2014, 2016), and the South Pole Telescope (SPT; Vieira et al. 2010; Mocanu et al. 2013). At longer radio wavelengths, surveys such as the Very Large Array (VLA) Faint Images of the Radio Sky at Twenty centimeters (FIRST) survey (Becker et al. 1995) and the Australia Telescope 20 GHz Survey (Murphy et al. 2010) provide important complementary data on the millimeter-bright AGN population. At shorter submillimeter/far-infrared wavelengths, the *Herschel* Space Observatory has undertaken the most comprehensive wide-field source surveys probing the DSFG population (e.g., Oliver et al. 2012; Viero et al. 2014; Valiante et al. 2016), with additional contributions from the Submillimetre Common-User Bolometer Array 2 (Holland et al. 2013; Geach et al. 2017). Complementing these $100+$ deg^2 surveys, there have been a host of smaller, deeper surveys by AzTEC at the JCMT and ASTE (e.g., Austermann et al. 2009, 2010), by the Max-Planck Millimeter Bolometer Array (MAMBO) and the Goddard-IRAM Superconducting 2 mm Observer (GISMO) on the IRAM 30 m telescope (e.g., Bertoldi et al. 2007; Lindner et al. 2011; Staguhn et al. 2014), by Bolocam at the CSO (e.g., Laurent et al. 2005), and by the Large APEX Bolometer Camera (LABOCA) on the APEX telescope (e.g., Greve et al. 2010).

The wide-field millimeter-wave surveys have modified our understanding of the blazar population. The first catalogs from ACT, *Planck*, and SPT provided unprecedented source count data at 150 GHz (2 mm) and 220 GHz (1.4 mm), spanning more than three orders of magnitude in flux density down to

10 mJy (Vieira et al. 2010; Marriage et al. 2011; Planck Collaboration et al. 2011a). To fit the new millimeter-wave data, Tucci et al. (2011) and others have introduced new models that inform classical models of blazar jets. Since then, expanded millimeter-wave catalogs have further constrained these new models (Mocanu et al. 2013; Marsden et al. 2014; Planck Collaboration et al. 2014, 2016; Datta et al. 2019).

The second millimeter-bright source population is composed of DSFGs. A subset of the strictly millimeter-selected DSFGs are local star-forming galaxies, which are bright in optical and infrared catalogs (e.g., Planck Collaboration et al. 2011b). However, the majority of the DSFGs detected in the millimeter-wave surveys to date correspond to lensed, high-redshift DSFGs (e.g., Negrello et al. 2007). The first detections at 1.4 mm were announced by SPT (Vieira et al. 2010), and subsequent work by ACT, *Planck*, and SPT has expanded the number of published millimeter-selected candidates to many hundreds (Mocanu et al. 2013; Marsden et al. 2014; Cañameras et al. 2015). As with classical SMGs, the UV and optical light from these galaxies is heavily obscured, leaving nearly all information about the sources in the far-infrared thermal dust spectra and accompanying molecular line spectra. Extensive complementary observations and modeling have established that the millimeter-selected DSFG population is magnified via gravitational lensing by typical factors of 5–10 with redshifts $z = 2$ –6, dust temperatures $T = 30$ –60 K, and significant dust optical depth at the peak of the thermal spectrum ($\lambda \approx 100 \mu\text{m}$ in the rest frame; e.g., Greve et al. 2012; Hezaveh et al. 2013; Vieira et al. 2013; Weiß et al. 2013; Cañameras et al. 2015; Harrington et al. 2016; Spilker et al. 2016; Strandet et al. 2016; Su et al. 2017). In addition to the millimeter-wave surveys, far-infrared surveys conducted by *Herschel* have provided extensive samples of DSFGs that are being similarly characterized and studied (e.g., Negrello et al. 2010; Busmann et al. 2013; Wardlow et al. 2013).

This work is part of a series of publications of millimeter-wave source catalogs from ACT. Marriage et al. (2011) and Marsden et al. (2014) provided catalogs of AGNs and DSFGs in the ACT southern survey centered at decl. -52° . Recently, Datta et al. (2019) published the first polarized source study from the ACTPol survey. Here we describe the detection and initial characterization of sources in the ACT equatorial survey (decl. 0° , range $\pm 2^\circ 2$). New to our approach is the addition of the ACT 277 GHz data, together with a multifrequency matched filter (MMF) to optimize DSFG detection across all three ACT frequency bands. Additionally, the presence of dust and CO emission from the Milky Way forces the introduction of systematic cuts for Galactic contamination. To handle the new source selection methods, we employ a new flux density debiasing technique described in Gralla & Marriage (2020) to account for Eddington bias, which is an important consideration for the faintest DSFGs. Enabled by the extra high-frequency channel and MMF, our sensitivity to DSFGs reaches a new level for a wide-field millimeter-wave survey. The rms equivalent 218 GHz standard error is 2–3 mJy, compared to 3–4 mJy in Mocanu et al. (2013) and Marsden et al. (2014). At this survey depth, a significant fraction of the recovered DSFGs are predicted to be unlensed high- z systems, similar to those probed by *Herschel* (e.g., Magnelli et al. 2012; Asboth et al. 2016; Nayyeri et al. 2016).

This paper is organized as follows. Section 2 introduces the ACT equatorial survey. How we processed the data to produce

²² For the purposes of this paper we will refer to all these synchrotron source classifications collectively as “AGNs” or “blazars.”

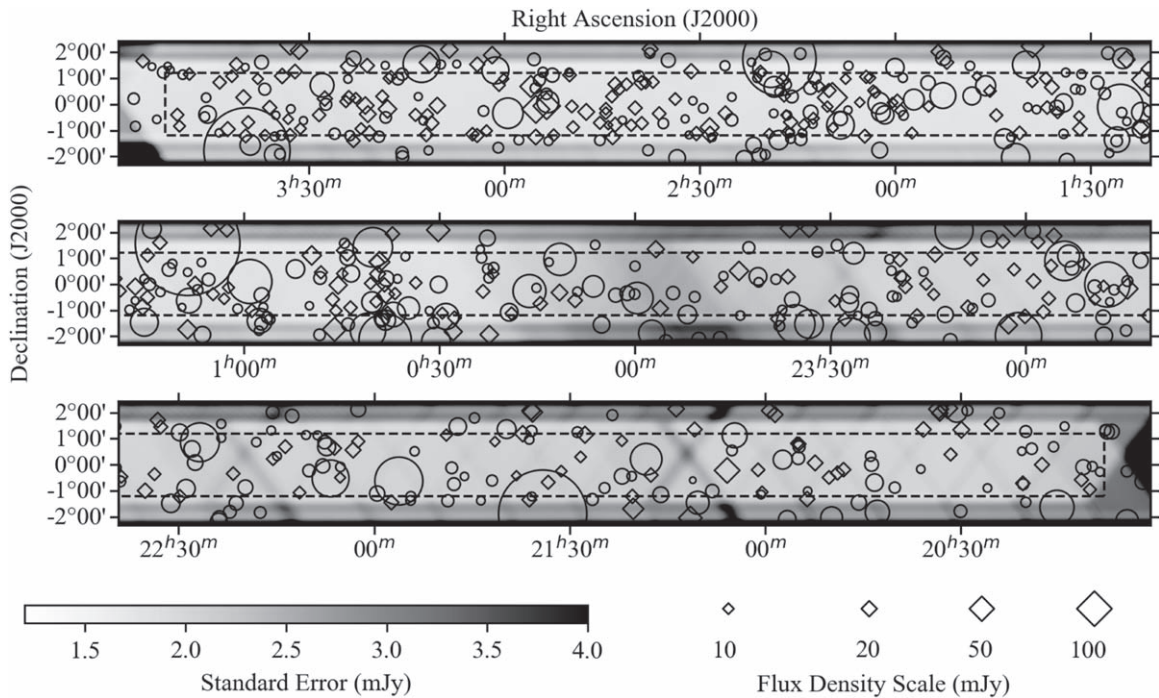


Figure 1. ACT equatorial source survey main field. The primary survey area, shown here split into three sections, spans 8 hr of R.A. along the celestial equator. A dashed rectangle bounds the subregion treated with the multifrequency matched filter optimized to identify DSFGs. The gray scale indicates the noise level of the data (standard error) for the 148 GHz matched-filtered data, which yield a similar sensitivity to the multifrequency filter (e.g., Figure 3). Diamonds (circles) show the locations of DSFGs (AGNs). The size of the symbol indicates the flux density, at 148 GHz for AGNs and at 218 GHz for DSFGs, with the scaling given in the lower right corner of the figure. There are additional fields with 148 GHz data centered at R.A. 8^{h} and 15^{h} (Figure 2).

catalogs is presented in Section 3, with the catalogs themselves presented in Section 4. The sources are characterized on the basis of their spectral properties, counts, and variability in Section 5, and a subsample of the brightest DSFGs that we have chosen for targeted follow-up is presented in Section 6. We conclude in Section 7. Throughout this work, α denotes the spectral index, relating flux density (S) to frequency (ν) according to $S(\nu) \propto \nu^\alpha$. In our bands, typical values are $\alpha = -0.7$ for synchrotron emission and $\alpha = 3.5$ for dust emission.

2. Data

ACT is a 6 m telescope located in the Atacama Desert at an elevation of 5190 m (Fowler et al. 2007). ACT’s first receiver was the Millimeter Bolometric Array Camera (MBAC; Swetz et al. 2011). Using the MBAC, ACT conducted surveys of the southern ($\delta = -52^\circ 12'$) and equatorial sky from 2008 to 2010. For these, ACT observed at three frequencies simultaneously: 148 GHz (2.0 mm), 218 GHz (1.4 mm), and 277 GHz (1.1 mm), with angular resolutions of $1'.4$, $1'.0$, and $0'.9$, respectively (Hasselfield et al. 2013b). The telescope has since been upgraded with two successive generations of polarization-sensitive receivers: ACTPol, described in Thornton et al. (2016), and Advanced ACTPol, outlined in Henderson et al. (2016). (MBAC was not polarization sensitive.) This paper presents point source catalogs from the MBAC-based equatorial survey. The 148 and 218 GHz data are from the 2009 and 2010 observing seasons, and the 277 GHz data are from the 2010 observing season.

Figure 1 shows the main ACT equatorial survey region used in this study. This region covers approximately 480 deg^2 on the celestial equator, with R.A. centered at 0^{h} and spanning from $19^{\text{h}}45^{\text{m}}$ to $4^{\text{h}}16^{\text{m}}$, and with decl. ranging from $-2^\circ 12'$ to $2^\circ 12'$.

There are, however, notable differences in survey coverage between bands. The survey region for the 277 GHz band, derived from only 1 yr of observations, is smaller than that of the lower-frequency bands. For the 148 GHz band, sources were identified in additional equatorial regions centered on R.A. 8^{h} and 16^{h} (Figure 2). These additional regions increase the survey area for 148 GHz by 360 deg^2 . Each map is produced with a cylindrical equal-area projection with its standard parallel at the equator, making a flat-sky approximation valid to well within errors across the narrow survey region. The square map pixels are $0.5'$ on a side at the equator. The maps used in this study are available on the Legacy Archive for Microwave Background Data Analysis.²³ In particular, the 277 GHz data set is newly released as of this publication.

For details about ACT observations and mapmaking procedures, see Dünner et al. (2013). In summary, each detector time stream is analyzed and either retained or rejected based on a number of criteria (i.e., weather, detector performance, etc.). A preconditioned conjugate gradient solver produces a maximum likelihood map from these time stream data. We fit for an initial estimate of the point source signals. Models constructed from these initial estimates are then subtracted from the time stream data, which are then processed into a new, noise-dominated maximum likelihood map. The source models are then added back into the final map. This two-step treatment of the map helps prevent source power from biasing noise estimates used to produce the final maps, which in turn prevents biasing the point source signal in the map solution.

The overall flux density calibration of the map for each band is determined from cross-correlation of the CMB power

²³ <https://lambda.gsfc.nasa.gov/>

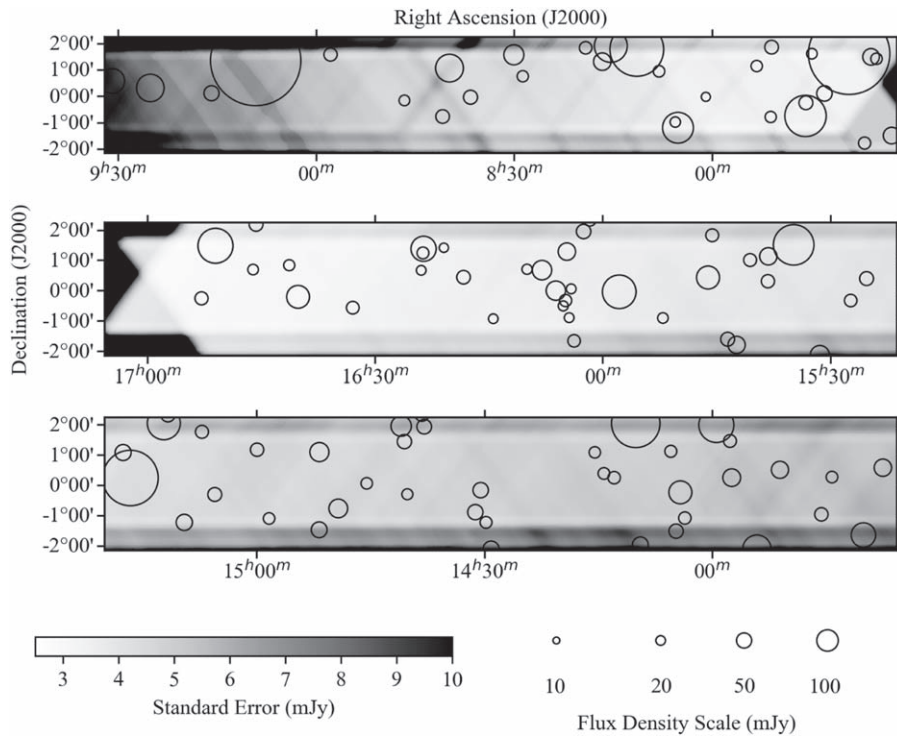


Figure 2. ACT equatorial source survey auxiliary fields. Auxiliary survey areas, one centered at R.A. 8^{h} (top panel) and the other at 16^{h} (bottom two panels), provide extra data at 148 GHz. The sources are marked by circles, with flux density indicated by the size of the circle. Although additional frequency bands are not available for spectral classification, at the flux density range probed by these data, the 148 GHz source population is dominated by AGNs (see Figure 13). The gray scale shows that these fields are shallower than the main field (Figure 1).

spectrum at $300 < \ell < 1100$ with that measured from the *Wilkinson Microwave Anisotropy Probe* (*WMAP*) using the deepest ACT maps (the 2010 season). The uncertainty on the absolute temperature calibration of the 148 GHz band to *WMAP* is 2% (at $\ell = 700$; Sievers et al. 2013; Hajian et al. 2011). Louis et al. (2014) cross-correlate the ACT maps with *Planck* maps and find excellent agreement.²⁴ The calibration is then transferred to the 218 GHz data through a cross-correlation with the 148 GHz map. Relative calibration between seasons is performed using cross-correlations between the data of each ACT season. Details of this process can be found in Das et al. (2014). In addition to the overall calibration uncertainties, errors in the assumed instrument beam and the mapmaking can propagate to uncertainty in the recovered ACT flux densities. As discussed in Gralla et al. (2014), the overall systematic uncertainties on the flux density measurements for the 148 GHz and 218 GHz bands are 3% and 5%, respectively. These uncertainties dominate statistical uncertainties for the brightest sources in our sample. The calibration of the 277 GHz band derives from observations of Uranus (Hasselfield et al. 2013b). Because this method is less accurate than the CMB-based calibration of the lower-frequency bands, the systematic error on the 277 GHz fluxes is 15%.

Part of the systematic flux density uncertainty is due to the fact that the telescope optical response depends on the source spectrum and whether the source is resolved (like the CMB) or point-like (e.g., Page et al. 2003; Swetz et al. 2011, Table 4). Publicly available ACT beams assume a CMB source spectrum, so their use in recovering point source flux density is nuanced. In particular, the effective center of the bandpass

for a given source depends on the convolution of its intrinsic spectrum with the instrument response over the band. As in Marsden et al. (2014), we have scaled the beam used in the matched filter and solid angle used in flux recovery to partially account for a shifted effective central frequency (148.65, 218.6, and 277.4 GHz for the three ACT bands). In Datta et al. (2019), a more detailed calculation was done to determine the range of flux density correction factors for different intrinsic source spectra. We have performed a similar analysis for the bands in this paper and estimated an associated systematic error in flux density recovery of 1.5%.

The ACT sensitivity varies throughout the maps according to the depth of coverage. Each map was filtered with the beam appropriate for that season and band, as described below. The resulting calibrated, filtered maps were combined into a multiseason map via a weighted average, with the weights set for a given pixel by the integrated time that that pixel was observed. Typical rms noise levels are 1.8, 2.4, and 5.2 mJy for 148, 218, and 277 GHz, respectively. Figure 1 shows the noise level across the main survey region for the 148 GHz band.

3. Methods

3.1. Spatial Matched Filtering

To optimize the signal-to-noise ratio (S/N) of the point-like sources, the ACT data were matched-filtered (e.g., Tegmark & de Oliveira-Costa 1998) with the ACT beam (Hasselfield et al. 2013b). The methods used are described fully in Marriage et al. (2011) and Marsden et al. (2014), which present catalogs of sources from the ACT southern surveys. Here we summarize the main steps of this analysis, with an emphasis on unique features of these new catalogs.

²⁴ The observed calibration factor between *WMAP* and *Planck* is 0.985, with *Planck* lower than *WMAP*.

The ACT brightness temperature map is first multiplied by a weighting function $W(\boldsymbol{\theta})$ proportional to the square root of the number of observations per pixel to make the white noise per pixel approximately constant across the survey region.²⁵ Because there are fewer observations toward the edge of the map, this produces an inverse-noise-weighted map of brightness temperature $T(\boldsymbol{\theta})$ with a tapered window function and Fourier transform $\tilde{T}(\mathbf{k})$.²⁶ This map is then filtered in the Fourier domain to produce a (weighted) matched-filtered map $T_{\text{MF}}(\boldsymbol{\theta})$:

$$T_{\text{MF}}(\boldsymbol{\theta}) = \int \exp(2\pi i \mathbf{k} \cdot \boldsymbol{\theta}) \Phi_{\text{MF}}(\mathbf{k}) \tilde{T}(\mathbf{k}) d\mathbf{k}, \quad (1)$$

where

$$\Phi_{\text{MF}}(\mathbf{k}) = \frac{F_{k_0, k_x}(\mathbf{k}) \tilde{B}^*(\mathbf{k}) |\tilde{T}_{\text{other}}(\mathbf{k})|^{-2}}{\int \tilde{B}^*(\mathbf{k}') F_{k_0, k_x}(\mathbf{k}') |\tilde{T}_{\text{other}}(\mathbf{k}')|^{-2} \tilde{B}(\mathbf{k}') d\mathbf{k}'} \quad (2)$$

is the matched filter. Angular features scale as $d\theta \approx \pi/k$ (in radians); e.g., $k = 3000$ corresponds to $3' - 4'$ where sources begin to dominate over the CMB power (see, e.g., Sievers et al. 2013). The function $\tilde{B}(\mathbf{k})$ (with units of steradian) is the Fourier transform of the “effective” instrument beam ($B(\boldsymbol{\theta})$), normalized such that $B(0) = 1$, which takes into account the dependence of the beam on the source spectrum and telescope pointing jitter (Section 3.1.1). The beam is well approximated as azimuthally symmetric ($\tilde{B}(\mathbf{k}) \approx \tilde{B}(k)$). The Fourier transform of the map data excluding the point sources, \tilde{T}_{other} , includes atmosphere, detector noise, the CMB, and any other sources of brightness temperature that represent noise for the source signal. Unlike $\tilde{B}(\mathbf{k})$, \tilde{T}_{other} is not azimuthally symmetric. As in Marsden et al. (2014), in practice $|\tilde{T}_{\text{other}}|^2$ is simply the power spectrum of the $W(\boldsymbol{\theta})$ -weighted temperature data, which approximates the noise sources given the low amount of power in the point sources. A high-pass filter, $F_{k_0, k_x}(\mathbf{k})$, eliminates undersampled modes below $k_0 = 1000$ and modes with $|k_x| < 100$, which are occasionally contaminated by telescope scan-synchronous noise.

Bright point sources in the maps can cause ringing from the matched filtering, which can introduce spurious low-S/N sources. We minimize this effect by initially searching for the brightest S/N > 50 sources, cataloging these, and removing them from the original maps by filling in a $25'$ radius around each source position with a uniform flux density equal to the typical map noise. For the 148 GHz selected sample, there are 41 such sources. We then refilter the maps without these bright sources, identifying all sources with S/N > 5 . The source candidates thus identified (both from the initial search and from the refiltered maps) are passed to the next phase of the analysis in which source location and flux density are reconstructed.

Before estimating the flux density from a filtered map, the map is divided by $W(\boldsymbol{\theta})$ to undo the weighting applied for source detection and multiplied by the beam solid angle Ω_B to

convert the brightness temperature to units of Jy beam⁻¹:

$$S_{\text{MF}} = W^{-1}(\boldsymbol{\theta}) \frac{\partial I_{BB}}{\partial T} T_{\text{MF}}(\boldsymbol{\theta}) \Omega_B, \quad (3)$$

where I_{BB} is the Planck intensity function. The partial derivative of I_{BB} evaluated at the CMB temperature converts the map T_{MF} from brightness temperature to intensity units, which are converted to flux density by the factor of the solid angle. For each detection, we extract a $0''.04$ -wide submap centered on the candidate source. In this submap, we remap the flux density from $0'.5$ pixels using Fourier interpolation (zero padding in \mathbf{k} space) into $16 \times$ smaller pixels ($\sim 2''$ on a side). The effect of averaging the source signal into pixels (“pixel windowing”) is also corrected. The new position and flux density estimation is associated with the maximum in the filtered map, now with finer pixelization. Finding a more accurate position for each source and correcting for pixel windowing is important for flux density recovery, especially for the higher-resolution 218 and 277 GHz bands and for sources that do not lie near the centers of the larger pixels in the original, filtered map. Examples of the matched-filtered data are shown in Figure 3.

3.1.1. Effective Multiseason Beams

The instrument beam transform $\tilde{B}(\mathbf{k})$ is measured separately for each observing band and season using observations of Saturn and Uranus (Hasselfield et al. 2013b). The spectral shape of these planets does not match that of most of the compact sources in this analysis, so the effective central frequency of the bands is shifted for each spectral shape (planets, CMB, AGNs, DSFGs). As reported by Swetz et al. (2011), the central frequencies are 147.6, 217.6, and 274.8 GHz for AGNs and 149.7, 219.6, and 277.4 GHz for DSFGs. To take into account that our source samples include both AGNs and DSFGs, we adopt fiducial central frequency values of 148.65, 218.6, and 277.4 GHz. These correspond to frequencies halfway between the central frequencies for steep-spectrum AGNs and DSFGs for the 148 and 218 GHz bands. For the 277 GHz band, we simply adopted the DSFG central frequency. The same 148 and 218 GHz central frequencies were used in our previous ACT compact source analysis (Marsden et al. 2014). We rescale the beam widths to account for the shifts in these new effective central band frequencies. For more information on the effects of the beam on the calibration uncertainty, see Section 2.

The effective instrument beam is also broadened owing to variations in pointing. We include this broadening by multiplying the instantaneous beam transform by $\exp(-k^2 \sigma_\theta^2 / 2)$, where $\sigma_\theta = 5''$ (Hasselfield et al. 2013b).

For 148 and 218 GHz, data from 2009 and 2010 were combined into single multiseason maps to increase the sensitivity to sources. These maps were filtered with the 2009 beams, but the choice of beam does not have a large effect. The FWHM of the beam changed by $< 5\%$ from 2009 to 2010 for all bands. To investigate how this change affects flux density recovery, we simulated sources to have the shape of the 2010 beam and added these sources to the 2010 map, but then we filtered this map with the 2009 beam. The flux densities recovered from this simulated map are lower than those input by 1%. Because in the analysis the actual source

²⁵ Over the course of the season, observations with high and low noise distribute in similar ratios across the map, making the number of observations per pixel a good proxy for the inverse of the resulting noise variance. This has been confirmed empirically.

²⁶ $\mathbf{k} = (k_x, k_y)$ is the angular wavevector, with x and y referring to R.A. and decl., respectively.

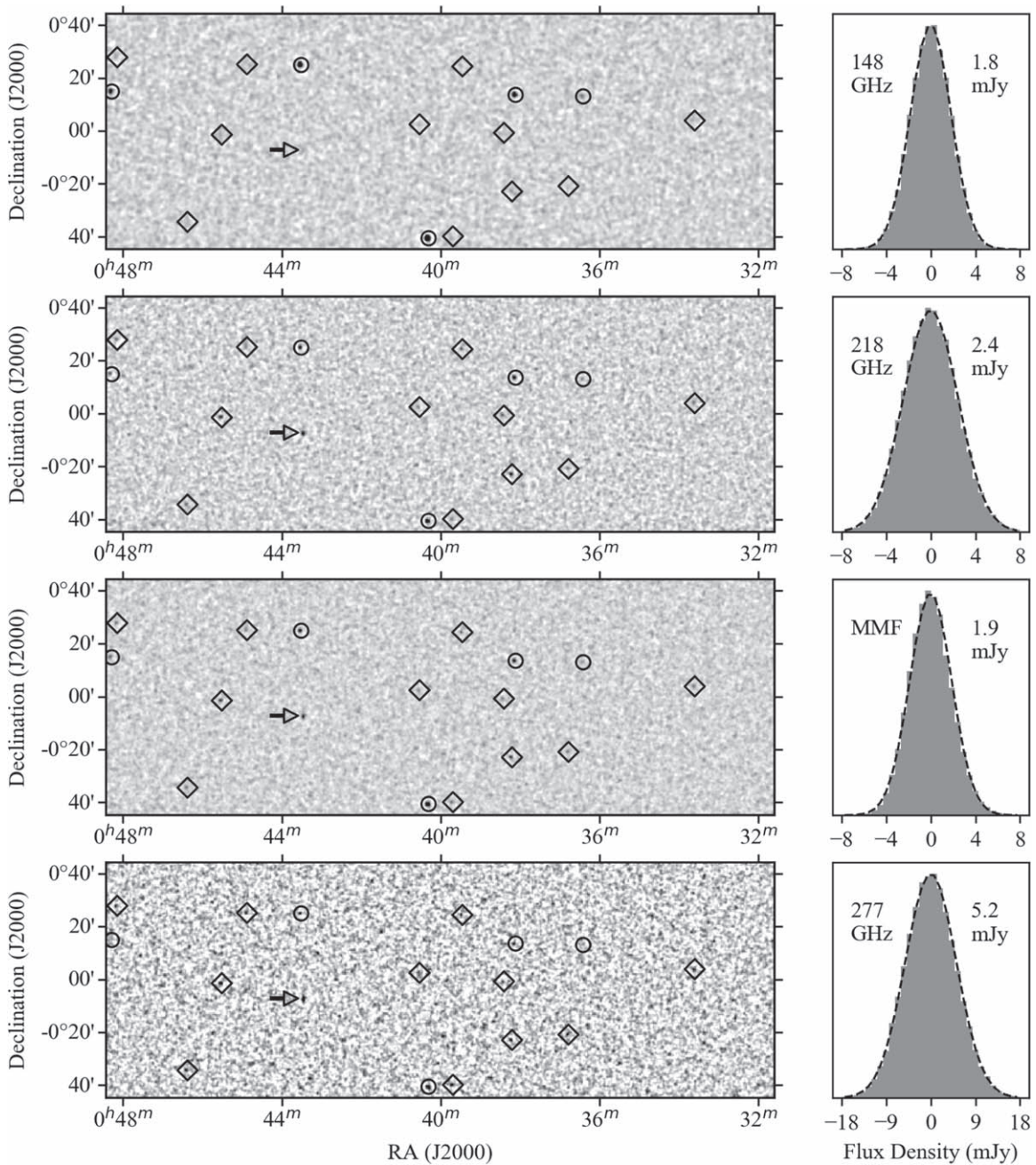


Figure 3. Filtered ACT data. From top to bottom on the left, a subregion is shown for the matched-filtered maps corresponding to 148 GHz, 218 GHz, the MMF, and 277 GHz. The MMF is optimized for a thermal dust spectrum and is referenced to 218 GHz. The grayscale limits (white to black) of the filtered map are -5 and 20 mJy. Sources detected with $S/N > 5$ are marked with circles for synchrotron-dominated emission and diamonds for dust-dominated emission. At right, the pixel flux density distribution functions are shown for each subregion with corresponding standard deviation values. The dashed line overlotted on each sample distribution is the Gaussian distribution with the sample standard deviation. A bright dust-dominated source at $00^{\text{h}}43^{\text{m}}27^{\text{s}}.8$ R.A. and $-0^{\circ}07'30''$ decl. (marked by a right-pointing arrow and most apparent in the 218 GHz and MMF maps) was rejected by the cuts for Galactic contamination. This source is the nearby late-type galaxy NGC 237 at $z = 0.014$. It was flagged for being more extended than 92% of all point sources with evidence for rest-frame CO (2–1) line emission. Other visible signals in these maps that are not marked are below the detection thresholds of any of the selection methods. See Table 1 for catalog entries for the sources in this figure.

shapes are some combination of the 2009 and 2010 beams, the flux densities of the sources in the multiseason catalogs are thus only affected at the subpercent level. The brightest sources in the catalogs are typically blazars, and their emission varies from one season to the next by more than 1% (Section 5.3). The faintest sources’ statistical uncertainties are larger than 1%. Thus, the effect from filtering the combined maps with the 2009 beams is not significant. Individual season flux densities, for which the 2010 map is filtered with

the 2010 beam, are also reported in the catalogs available online.

3.2. Multifrequency Matched Filtering

To improve sensitivity to sources beyond the spatial matched filtering described above, we use the multifrequency information available from ACT. The methods we use extend beyond what has previously been done with ACT data. In this work, we

specifically construct an MMF (e.g., Melin et al. 2006) to search for faint, dusty galaxies. This choice is motivated by the availability of the 277 GHz data. Blazar detections are statistically dominated by the 148 GHz band, obviating the need for an MMF. However, both the 218 and 277 GHz bands contribute significantly to the filtered DSFG signal, motivating the MMF for DSFG selection.

The MMF optimizes the S/N of a point source using data across multiple bands. As formulated in this work, the MMF produces a single map $T_{\text{MMF}}(\boldsymbol{\theta})$ at a reference frequency ν_0 from multiple maps $\{T_\nu(\boldsymbol{\theta})\}$ at multiple frequencies $\{\nu\}$. By analogy with the single-frequency matched filter (Equation (1)), the MMF map is generated by applying a multicomponent filter to the multifrequency map set $\{T_\nu(\boldsymbol{\theta})\}$:

$$T_{\text{MMF}}(\boldsymbol{\theta}) = \int \exp(2\pi i \mathbf{k} \cdot \boldsymbol{\theta}) \sum_{\nu} \Psi_{\nu}(\mathbf{k}) T_{\nu}(\mathbf{k}) d\mathbf{k}, \quad (4)$$

where, in the fully general case, the filter functions $\Psi_{\nu}(\mathbf{k})$ account for correlated noise between bands (e.g., correlations due to common modes from the CMB and atmospheric emission in ACT data). In principle, these correlations enter the formulation of the filter. In practice, for source selection at arcminute resolution, the strongly correlated modes at large angular scales can be neglected relative to the more abundant small angular scale modes that are dominated by uncorrelated detector noise. The interband correlations from the CMB and the atmosphere dominate the uncorrelated detector noise for wavevectors $k < 3000$, corresponding to angular scales $> 3' - 4'$. Given the arcminute resolution of the ACT 218 and 277 GHz bands, approximately 10 ACT beams fit within a correlated patch. In other words, there are 10 times more beam-sized modes than modes for which CMB or atmosphere dominates. The effects of correlations are further minimized by the extra high-pass filter F_{k_0, k_x} in Equation (2), which de-weights the relatively few modes with $k < 1000$. There remains residual correlated noise at high k (e.g., the unresolved cosmic infrared background) in the filtered ACT maps that presents a correlated noise source, but it is subdominant to detector noise. This is reflected by correlation coefficients: 0.13 between 148 and 218 GHz, 0.17 between 218 and 277 GHz, and 0.09 between 148 and 277 GHz. Thus, significant gains in S/N are achieved with a simplified filter that assumes independent interband noise.

With independent interband noise, the MMF map (Equation (4)) takes a simple, intuitive form. Working in units of flux density per beam (Equation (3)), the MMF map is the weighted combination of the single-frequency matched-filtered maps $\{S_{\text{MF};\nu}\}$ corresponding to the linear least-squares best estimate of the flux density at the reference frequency:

$$S_{\text{MMF};\nu_0}(\boldsymbol{\theta}) = \sum_{\nu} w_{\nu}(\boldsymbol{\theta}) S_{\text{MF};\nu}(\boldsymbol{\theta}), \quad (5)$$

where the weights w_{ν} are

$$w_{\nu}(\boldsymbol{\theta}) = \sigma_{\text{MMF}}^2(\boldsymbol{\theta}) \frac{f_{\nu}}{\sigma_{\nu}^2(\boldsymbol{\theta})}. \quad (6)$$

In this equation, $\sigma_{\nu}^2(\boldsymbol{\theta})$ is the (position-dependent) flux density variance in the single-frequency matched-filtered map for frequency ν . The constant f_{ν} encodes the assumed spectral energy distribution (SED) of the source, relating the flux

density S_{ν} at frequency ν to the flux density S_{ν_0} at the reference frequency ν_0 :

$$f_{\nu} = \frac{S_{\nu}}{S_{\nu_0}} = \left(\frac{\nu}{\nu_0}\right)^{\alpha}. \quad (7)$$

Finally, $\sigma_{\text{MMF}}^2(\boldsymbol{\theta})$ is the variance in the MMF map:

$$\sigma_{\text{MMF}}^2(\boldsymbol{\theta}) = \left(\sum_{\nu} \frac{f_{\nu}^2}{\sigma_{\nu}^2(\boldsymbol{\theta})} \right)^{-1}. \quad (8)$$

Therefore, given the dominance of independent noise between ACT frequency bands, we can use this simplified formalism, availing ourselves of the tools developed for the single-frequency matched filter described in Section 3.1.

For DSFGs, we take the 218 GHz map as the reference data set and optimize the multifrequency combination for a typical dusty source spectrum with spectral index $\alpha = 3.77$. Thus, the frequency scale factors (Equation (7)) are $f_{148} = 0.232$, $f_{218} = 1.00$, and $f_{277} = 2.47$. The multifrequency map generated was restricted to the region between $20^{\text{h}}09^{\text{m}}$ and $03^{\text{h}}51^{\text{m}}$ in R.A. and between $-1^{\circ}33'$ and $1^{\circ}24'$ in decl., where there was adequate coverage in the 277 GHz data. Filtered data in a subregion of the MMF area are shown in Figure 3 for the three single-frequency maps and the MMF map. Equation (8) predicts a noise level in the MMF, referenced to 218 GHz, of 1.6 mJy; however, the measured level is 1.9 mJy (compared to the 2.4 mJy noise in the single-frequency map). The full sensitivity improvement is not achieved owing to residual noise correlations between bands, which make Equation (6) sub-optimal. In the end, the cleanest comparison between the MMF and 218 GHz single-frequency approach is in terms of S/N: for DSFGs in the MMF-derived catalog (Section 4), the median improvement in S/N of the MMF over the 218 GHz data alone is 1.30.

3.3. Detection, Selection, Localization, and Flux Density Recovery

In Section 4, we introduce a catalog in which sources are detected in multiple maps. As discussed in Section 3.1, a source is detected in a map if its S/N > 5 . By this definition, a source may be detected in a combination of single-frequency filtered maps and the MMF map tuned for a dust-like spectrum. We further identify each source with the data set in which it is detected with the highest S/N. This ‘‘selection map’’ defines the selection function and also provides the most precise location of the source. The data set in which a source is selected also plays into flux density debiasing (Section 4.3).

To estimate flux densities and associated errors, the single-frequency filtered maps $T_{\text{MF};\nu}$ are used. In a $4'$ patch centered on each source, the map $T_{\text{MF};\nu}$ is reprojected with Fourier interpolation to ($\sim 2''$) pixels, correcting for the signal-dilution effect of the pixel window function. Then, the flux density is obtained from this finer-pixelized map at the selection-map-determined source location (i.e., by ‘‘forced photometry’’). Thus, even if a source is undetected in a single-frequency map, it will still have an associated (low-S/N) flux estimate.

Note that if the selection map is itself a single-frequency map, then that map will be used to determine the source’s selection function, location, and flux density. The MMF map is never used for flux density estimation, only source selection

and localization. Conversely, due to its high noise, the 277 GHz map is never used for selection or localization.

4. Catalogs

4.1. Overview

We present the ACT equatorial extragalactic and Galactic source catalogs based on detections in three different maps.²⁷ As discussed in Section 3.3, sources are said to be detected in a map if they have an $S/N > 5$. The source is said to be “selected” in the map in which it has the highest S/N . Thus, each source is uniquely identified with one of the following groups:

1. The first subset of sources is selected from the single-frequency matched-filtered 148 GHz data. The 148 GHz selection is typically most sensitive for sources with flat or falling spectra such as AGNs. Finally, we note that the 148 GHz selection includes the auxiliary fields shown in Figure 2 and that the sources in these fields lack coverage in the other ACT bands.
2. The second group of sources is selected using a three-frequency MMF map. As discussed in Section 3.2, the MMF is optimized for sources with a dust SED, and the resulting map is limited by the footprint of the 277 GHz map, which is smaller than the 218 GHz coverage. Informed by the simulations of catalog completeness (Section 4.3), we further limit our MMF selection to the most sensitive part of the MMF map, within the decl. range $-1^{\circ}12'$ to $1^{\circ}12'$.
3. The third source selection is based on the single-frequency matched-filtered 218 GHz data outside the sky region used for MMF selection. Like the MMF map, the 218 GHz data provide more sensitivity to DSFGs than the 148 GHz data.

Sources in the equatorial catalog are tested for Galactic dust or CO emission according to automated methods (Section 4.2), which flag 321 detections as being likely of Galactic origin. These sources are provided in the Galactic catalog. Because the Galactic contamination cuts rely on multifrequency data and mainly affect the MMF and 218 GHz selection, all flagged sources are in the main survey field (Figure 1). Excluding these sources, the total number of sources in the extragalactic catalog is 797. Of these, 112 sources lie in the auxiliary fields (Figure 2) with only 148 GHz data. In terms of selection, the 148 GHz, MMF, and 218 GHz methods described above yield 504, 217, and 76 extragalactic sources, respectively.

Based on their spectral properties (Section 5.1), 268 sources are labeled in the catalog as DSFGs, and 376 sources are identified as AGNs. Of the 268 DSFGs, 200 sources were MMF selected and 68 sources were 218 GHz selected. No sources classified as DSFGs were 148 GHz selected. Analogously, only 5% of the AGN-classified sources were selected in the 218 GHz (0) and MMF (6) maps. The vast majority (370) of the 376 AGNs are 148 GHz selected.

The remaining sources lack the requisite multifrequency information for spectral classification. They are flagged in the catalog as AGN* (134 sources; mostly from auxiliary fields) or DSFG* (19 source) based on whether they are detected only at

148 GHz or 218 GHz. (MMF-selected sources, by definition, have enough multifrequency data for spectral classification.)

To identify DSFGs that have nearby dusty galaxy counterparts, we visually inspected $50''$ cutouts from the Sloan Digital Sky Survey (SDSS; Alam et al. 2015) of all sources in the sample, including those our automated algorithm identified as Galactic. There is an additional flag in the catalog for these nearby galaxies, and their ACT spectral index distribution is discussed in Section 5.1. We additionally flag three sources that may correspond to stars with associated radio or far-infrared emission. In total, 68 sources in the extragalactic catalog are flagged as likely local galaxies or stars, and 12 sources in the Galactic catalog are flagged. An example of this is shown in Figure 3 for NGC 237 at $z = 0.014$.

Source data provided in the extragalactic catalog include source ID, position, and S/N based on the selection map, raw and debiased flux densities, raw and debiased spectral indices, AGN/DSFG classification, statistics associated with Galactic cuts, and the local galaxy flag.²⁸ For 148 GHz selected sources in the extragalactic catalog, we additionally provide raw flux density estimates from data in 2009 and 2010 separately. All 148 GHz selected sources are AGNs, and the per-year flux densities give a handle on AGN variability (Section 5.3). In the Galactic catalog we provide the same data as in the extragalactic catalog excluding debiased flux densities and spectral indices and per-year flux density estimates. A sample of the extragalactic catalog for sources shown in Figure 3 is given in Table 1.

4.2. Removing Dusty Galactic Emission

In addition to the extragalactic sources of interest in this study, ACT also detects Galactic dust emission, particularly in the 218 and 277 GHz data. Galactic CO emission may also contaminate the 218 GHz band. There is more Galactic contamination at the eastern and western edges of the maps (R.A. $> 03^{\text{h}}45^{\text{m}}$ and R.A. $< 20^{\text{h}}15^{\text{m}}$), where large Galactic structures are clearly visible. The source-finding algorithm, although optimized for point sources, also identifies bright regions of extended emission as sources. To distinguish true extragalactic sources from the Galactic emission, we characterize the sources by their shapes, SED, and clustering properties. We also use information from *Planck* to identify regions of the sky with high Galactic dust emission.

With the exception of nearby galaxies (e.g., NGC 1055), extragalactic sources tend to be unresolved by the ACT beams (FWHM $0'.9$ to $1'.4$). We characterize the shapes of the sources in the following way. Starting with the filtered detection map, for each source we create a submap with upgraded pixel resolution ($\sim 2''$) and Fourier interpolation (zero padding) of the data. In this submap we identify the pixel with the peak brightness and normalize all pixels in the submap by that value. The resulting submap has pixel values that are fractions of the peak value. We then sum the normalized pixel values in a $2'.5$ square around that peak, calling the result the “extended index.” By this definition, the extended index is a simple metric that increases with the solid angle subtended by the source (albeit in a filtered map). We note that although the extended index is defined within $2'.5$, sources that are even larger are also likely to have a large extended index because they are unlikely

²⁷ Catalogs are available for download at the NASA Legacy Archive for Microwave Background Data Analysis (<https://lambda.gsfc.nasa.gov/>).

²⁸ Debiasing is not performed for 148 GHz selected sources above 50 mJy, where the effect is negligible. In these cases the debiased flux density is not left blank in the catalog but reported as the (equivalent) raw flux density for ease of catalog use.

Table 1
Sample of the Extragalactic Catalog^a

ACT-S ID ^b (J2000)	S/N	Selection ^c	α_{148}^{218d}	$\alpha_{148}^{277}/\alpha_{218}^{277e}$	Type ^f	S_{148} (mJy)	S_{218} (mJy)	S_{277} (mJy)
003337+000353	6.4	MMF	3.2 (3.0 ^{+1.6} _{-1.4})	3.6 (3.5 ^{+1.4} _{-1.3})	DSFG	3.5 ± 1.8 (2.7 ^{+1.6} _{-1.3})	12.2 ± 2.8 (8.8 ^{+3.7} _{-3.2})	28.7 ± 5.4 (22.7 ^{+5.3} _{-5.2})
003626+001301	6.4	148	0.2 (0.1 ^{+0.7} _{-0.7})	-0.6 (-1.1 ^{+1.2} _{-1.9})	AGN	11.9 ± 1.9 (10.7 ^{+2.2} _{-2.3})	12.9 ± 2.8 (11.4 ^{+2.6} _{-2.5})	8.3 ± 5.7 (5.2 ^{+5.6} _{-3.6})
003648-002052	5.9	MMF	4.1 (3.5 ^{+1.7} _{-1.5})	3.5 (3.3 ^{+1.5} _{-1.4})	DSFG	2.3 ± 1.8 (2.0 ^{+1.4} _{-1.4})	11.7 ± 2.8 (8.4 ^{+3.6} _{-3.0})	26.6 ± 5.6 (20.3 ^{+5.3} _{-5.2})
003808+001334	20.3	148	-0.3 (-0.3 ^{+0.3} _{-0.3})	-0.7 (-0.8 ^{+0.4} _{-0.5})	AGN	37.4 ± 1.8 (37.1 ^{+2.5} _{-2.3})	33.3 ± 2.7 (32.9 ^{+2.7} _{-2.7})	23.4 ± 5.8 (21.8 ^{+6.0} _{-6.0})
003814-002255	10.7	MMF	3.0 (3.0 ^{+0.8} _{-0.7})	1.9 (2.0 ^{+0.9} _{-0.8})	DSFG	7.6 ± 1.8 (7.1 ^{+1.8} _{-1.7})	24.6 ± 2.7 (23.5 ^{+2.7} _{-3.8})	39.1 ± 5.5 (36.9 ^{+5.3} _{-5.3})
003826-000044	6.0	MMF	4.4 (3.7 ^{+1.5} _{-1.4})	1.0 (1.7 ^{+1.6} _{-1.3})	DSFG	2.9 ± 1.8 (2.6 ^{+1.5} _{-1.3})	15.7 ± 2.7 (11.8 ^{+3.9} _{-4.3})	20.2 ± 5.5 (15.3 ^{+4.8} _{-4.6})
003929+002422	8.9	MMF	3.2 (3.1 ^{+1.1} _{-1.0})	2.1 (2.2 ^{+1.1} _{-1.0})	DSFG	5.7 ± 1.8 (5.1 ^{+1.8} _{-1.7})	20.0 ± 2.7 (17.7 ^{+3.9} _{-4.5})	33.4 ± 5.5 (29.9 ^{+5.3} _{-5.2})
003943-003952	6.6	MMF	4.4 (3.6 ^{+1.7} _{-1.5})	4.0 (3.9 ^{+1.4} _{-1.2})	DSFG	2.2 ± 1.8 (2.0 ^{+1.4} _{-1.0})	12.1 ± 2.7 (8.6 ^{+3.7} _{-3.1})	31.8 ± 5.5 (26.2 ^{+5.4} _{-5.3})
004020-004035	37.1	148	-0.8 (...) ^g	-0.5 (...)	AGN	68.5 ± 1.8 (68.5 ^{+1.8} _{-1.8})	49.4 ± 2.8 (49.4 ^{+2.8} _{-2.8})	51.2 ± 5.8 (51.2 ^{+5.8} _{-5.8})
004033+000228	5.6	MMF	2.7 (2.6 ^{+1.5} _{-1.3})	2.7 (2.6 ^{+1.5} _{-1.3})	DSFG	4.1 ± 1.8 (3.1 ^{+1.7} _{-1.3})	11.7 ± 2.7 (8.4 ^{+3.6} _{-3.0})	22.0 ± 5.5 (15.7 ^{+5.0} _{-4.7})
004332+002456	24.5	148	-0.8 (-0.8 ^{+0.3} _{-0.3})	-0.3 (-0.3 ^{+0.3} _{-0.3})	AGN	45.1 ± 1.8 (44.7 ^{+2.6} _{-2.6})	32.8 ± 2.7 (32.6 ^{+2.7} _{-2.7})	37.6 ± 5.8 (36.6 ^{+5.8} _{-5.7})
004454+002509	5.8	MMF	4.7 (3.8 ^{+1.7} _{-1.5})	4.4 (3.7 ^{+1.4} _{-1.3})	DSFG	1.6 ± 1.8 (1.7 ^{+1.2} _{-0.9})	10.1 ± 2.7 (7.8 ^{+3.4} _{-2.6})	28.7 ± 5.5 (22.3 ^{+5.4} _{-5.2})
004532-000127	11.1	MMF	3.8 (3.8 ^{+0.9} _{-0.8})	2.1 (2.1 ^{+0.9} _{-0.8})	DSFG	5.9 ± 1.8 (5.6 ^{+1.7} _{-1.7})	25.9 ± 2.8 (25.0 ^{+3.5} _{-4.3})	42.4 ± 5.6 (40.7 ^{+5.4} _{-5.3})
004624-003424	6.4	MMF	4.7 (3.8 ^{+1.6} _{-1.4})	2.1 (2.4 ^{+1.5} _{-1.4})	DSFG	2.4 ± 1.8 (2.2 ^{+1.5} _{-1.1})	15.2 ± 2.8 (11.1 ^{+4.0} _{-4.6})	25.1 ± 5.5 (19.7 ^{+5.1} _{-5.0})
004810+002750	6.3	MMF	1.8 (1.6 ^{+1.1} _{-1.1})	2.3 (2.5 ^{+1.5} _{-1.3})	DSFG	6.7 ± 1.8 (5.7 ^{+1.8} _{-1.9})	13.3 ± 2.8 (9.5 ^{+3.9} _{-3.9})	23.1 ± 5.5 (17.2 ^{+5.1} _{-4.9})
004818+001452	13.7	148	-1.1 (-1.0 ^{+0.4} _{-0.3})	-2.1 (-2.4 ^{+1.0} _{-1.4})	AGN	25.4 ± 1.9 (24.6 ^{+2.6} _{-2.6})	16.9 ± 2.8 (16.7 ^{+2.5} _{-2.5})	6.6 ± 5.8 (5.5 ^{+5.0} _{-3.3})

Notes.

^a The entries in this catalog sample correspond to the sources found in the data shown in Figure 3. Only a subset of columns in the full catalog are shown.

^b The ACT-S ID encodes the sexagesimal position of each source (hhmmss ± ddmms).

^c The selection data set is that in which the source is detected with the highest S/N (listed at left).

^d For interband spectral indices (α_{λ}^{ν}) and flux densities (S_{λ}), raw (debiased) values are given outside (inside) parentheses.

^e For 148 GHz selected sources, we report α between 148 and 277 GHz, whereas for MMF and 218 GHz selection, we report α between 218 and 277 GHz.

^f The type of source is designated as an AGN (DSFG) if the 148–218 GHz spectral index is less than (greater than) unity as described in Section 5.1.

^g Debiasing is not computed for 148 GHz selected sources with $S_{148} > 50$ mJy. Therefore, debiased spectral indices are not provided. For ease of catalog use, raw flux densities are reported in the debiased flux density columns. For this class of bright source, the raw and debiased estimates of flux densities are equivalent.

to have pixel distributions as concentrated as the beam shape within the $2\frac{1}{5}$ submap.

Because of its spectral shape and extended morphology, Galactic dust is not a strong contaminant for low-frequency, high-resolution interferometric radio surveys. Thus, ACT sources with counterparts in the VLA FIRST survey are more likely to be extragalactic than Galactic. We calculate the cumulative distribution of the extended indices of sources with FIRST counterparts. This cumulative distribution defines a scale for judging the extended index. For each source we define the “extended percentile” as the fraction of ACT sources with FIRST counterparts that are more compact (smaller extended index) than that source. For example, an ACT source with an extended percentile of 0.98 has a larger extended index than 98% of the FIRST sources in the map.

Because extended Galactic emission is often resolved into clustered groups of sources, many of the Galactic sources have

multiple neighbors nearby. For each source, we compute the number of neighboring sources within a $0\frac{5}{8}$ radius. To contextualize this metric, we calculated the number of neighbors for random positions throughout the map. The correlation lengths of lensed DSFGs and AGNs are long enough that a random position approximation holds for this purpose. The fraction of randomly located sources with more than four neighbors is only 0.03. On the other hand, the fraction of detected sources with more than four neighbors is 0.19, motivating the cuts for contamination described below.

We also investigated the spectral properties of the sources, particularly in the region that has information in all three frequency bands. Details of the spectral index distributions of the ACT sources are presented in Section 5.1. Galactic dust contamination is expected to have a dust-like spectrum ($\alpha > 3$). Additionally, we find that many of the sources identified as clearly Galactic dust contamination have excess

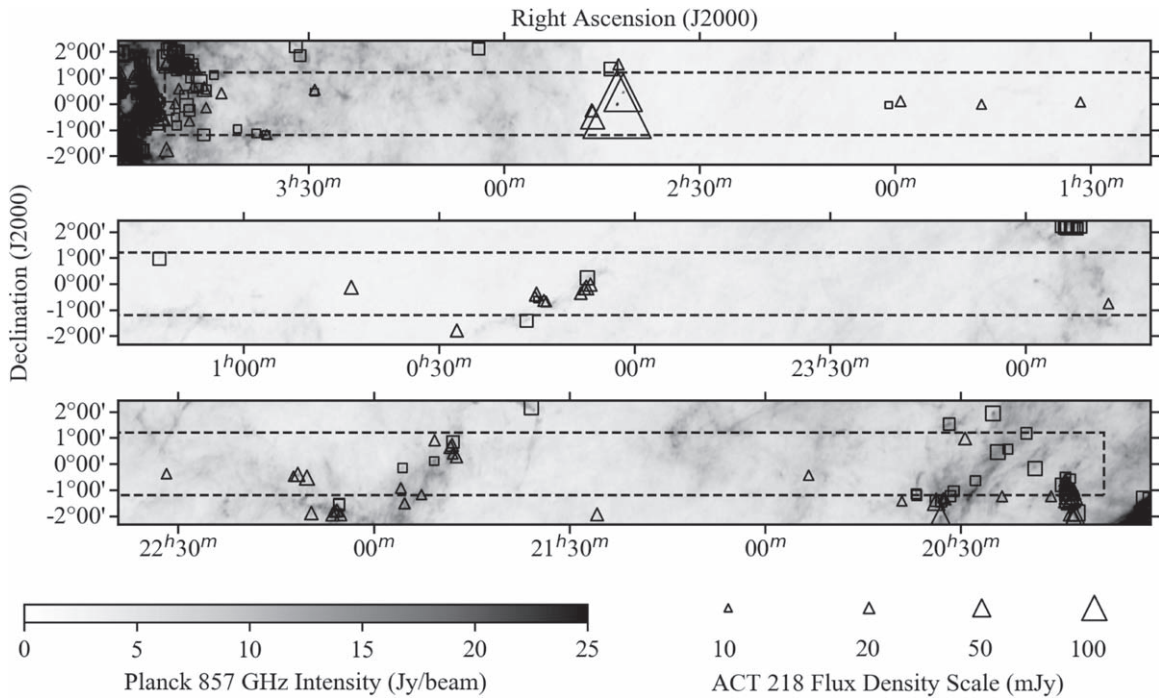


Figure 4. Source detections flagged by Galactic contamination cuts. Sources were selected as potential Galactic contamination based on combinations of criteria (Section 4.2) including compactness, clustering, CO (2–1) emission, and location in regions of high *Planck* 857 GHz intensity (shown in gray scale). Sources with evidence of CO contamination are shown as triangles, whereas other sources, generally (but not exclusively) with dust-like spectra, are shown as squares. A dashed rectangle bounds the subregion treated with the multifrequency matched filter optimized to identify DSFGs. The sizes of the symbols indicate the ACT 218 GHz flux densities. The 321 sources flagged as Galactic are not included in the extragalactic catalog (Figures 1 and 2) but are provided in a separate catalog.

emission in the 218 GHz band. Thus, their spectral indices from 148 to 218 GHz are positive (and significantly larger than $\alpha = 3$ or 4 characteristic of dust), while their spectral indices from 218 to 277 GHz are negative. This excess emission is likely caused by bright spectral line emission from CO (2–1) at 230.538 GHz. The ACT band extends from a half-power point of 210 GHz to a half-power point of 230 GHz (see Figure 9 in Swetz et al. 2011), with the response being a steep function of frequency. As discussed below, we only use this spectral information in conjunction with other measures (morphology and clustering) to flag sources as Galactic. Thus, compact, isolated extragalactic sources that may have unusual spectra remain in the catalog.

We visually inspected the sources in the map to develop criteria for removing Galactic dust contamination based on the measurements described above. These choices are informed by the properties of the clearly Galactic sources in dust complexes such as those at R.A. $03^{\text{h}}50^{\text{m}}$, $00^{\text{h}}11^{\text{m}}$, and $20^{\text{h}}13^{\text{m}}$. We apply four different cuts for Galactic contamination based on the MMF or 218 GHz data. (1) We remove as Galactic contamination all MMF and 218 GHz detected sources with both $\alpha_{148-218} > 1$ and $\alpha_{218-277} < 1$ (a proxy for CO contamination) that also either have more than four neighbors or have extended percentiles greater than 0.8. There are 169 sources that are flagged by this cut. (2) We also remove all MMF and 218 GHz detections that have more than four neighbors and extended percentiles greater than 0.8. This cut flags 195 sources. It removes an additional 76 beyond the initial cut. (3) For sources that lie within areas of the *Planck* 857 GHz map with intensity above 6 MJy sr^{-1} (as determined from an adjacent pixel to reduce bias from the source itself), we apply a more restrictive cut that removes sources with MMF or 218 GHz based extended percentile greater than 0.5 or that

have more than four neighbors and evidence for CO. This third set of criteria flags 262 sources. It removes an additional 49 sources beyond the first two cuts. (4) We flag sources as Galactic if they are extreme in terms of number of neighbors (≥ 10) or extended percentile (> 0.995). This identifies an additional 18 sources as Galactic. In addition to these cuts based on 218 GHz or MMF data, we remove sources detected *only* at 148 GHz that lie within $0^{\circ}.12$ of sources that are detected at either 218 GHz or in the MMF map and are identified as Galactic by the above criteria or that have a 148–218 GHz spectral index > 2 . This cut removes an additional 9 sources. In all, 321 sources are flagged as Galactic contamination. These sources are shown superposed on the *Planck* 857 GHz data in Figure 4. Among the sources flagged as Galactic, the 148 GHz, MMF, and 218 GHz selection methods (Section 4) are associated with 13, 82, and 226 sources, respectively. The fact that the majority of sources flagged as Galactic originate with the 218 GHz selection follows from the facts that Galactic cirrus is faint at 148 GHz and that many of the cirrus complexes seen in Figure 4 fall outside the MMF region. Additionally, the MMF selection is less susceptible to CO emission, because it does not rely solely on the contaminated 218 GHz band. Of the 321 flagged sources, a majority (178) show evidence (according to the criterion in cut 1) of CO contamination.

The Galactic contamination cuts that we have implemented need to be aggressive enough to ensure purity of the DSFG sample, but also surgical enough to leave the vast majority of DSFGs. For instance, after the cuts, the fraction of sources in the extragalactic catalog with more than four neighbors within $0^{\circ}.5$ is reduced to 0.01 from 0.19 (compared to 0.03 for random locations). Similarly, before the cuts, the fraction of sources with an extended percentile exceeding 0.95 is 0.25, significantly higher

Table 2
ACT Equatorial Catalog Summary

	Extragalactic Catalog ^a	Galactic Catalog
Total detections	797	321
148 GHz selection ^b	504	13
MMF selection	217	82
218 GHz selection	76	226
In auxiliary fields ^c	112	N/A
DSFG ^d	268	N/A
AGN	376	N/A
DSFG*	19	N/A
AGN*	134	N/A
CO ^e	N/A	178
Nearby galaxy/star ^f	68	12

Notes.

^a The full source sample is divided into extragalactic and Galactic catalogs based on cuts for Galactic contamination (Section 4.2).

^b Selection methods correspond to the map in which a source has the highest significance (Section 4).

^c Auxiliary fields, with only 148 GHz data, are shown in Figure 2.

^d Distinction between DSFG and AGN is based on spectral information (Section 5.1), whereas DSFG* and AGN* denote sources lacking spectral information but sorted into source category based on the detection map (most are from auxiliary fields). Typical source spectral indices are listed in Table 4.

^e CO indicates a spectrum in sources flagged as Galactic that is indicative of CO (2–1) emission (Section 4.2).

^f This flag denotes sources that lie within 50'' of a nearby ($z < 0.1$) galaxy in SDSS or by one of three radio/far-infrared-bright stars.

than the 0.05 fraction expected if all sources were point-like. After the Galactic contamination cuts, the fraction of sources with extended percentile exceeding 0.95 is reduced to 0.05. To further check that Galactic cuts are effective, we investigated the effect of the cuts on the number counts of the remaining sources. As discussed in Section 5.2.1, we calculated the number counts separately for regions of the map that are relatively free of Galactic dust emission and for those that underwent significant cleaning (in which one might expect extra false positives if the Galactic cuts were inadequate). We found that the number counts are statistically consistent between these different regions.

Since we have erred on the side of caution with the Galactic contamination cuts, some extragalactic systems will be flagged. For instance, nearby star-forming galaxies (such as NGC 237 in Figure 3) may be cut owing to significant CO (2–1) emission in the 218 GHz band (e.g., Figure 3 of Gralla et al. 2014) and extended brightness profiles. And while sources at higher redshift will neither be extended nor suffer significant CO contamination, they may be removed by chance. Below in Figure 6, we nevertheless show that we flagged and removed unresolved extragalactic sources at the few-percent level, based on how many randomly distributed simulated sources are flagged. Summaries of the extragalactic and Galactic catalogs are given in Table 2.

4.3. Debiasing and Completeness

4.3.1. Debiasing Method and Description of Simulations

The flux densities of sources recovered from a population with steeply falling number counts are biased high relative to

their intrinsic flux densities. In the sub/millimeter wavelength community, correcting for this bias is referred to as “deboosting” (e.g., Coppin et al. 2005). Motivated in part by the presence of Galactic dust in these equatorial maps and the methods we developed to remove them from the catalog, we developed a new method to perform this deboosting based on injecting simulated sources into the maps. We refer to our methods as “debiasing” rather than deboosting to distinguish our treatment, which can correct flux densities either up or down, from traditional deboosting. We describe in detail these methods in an accompanying paper (Gralla & Marriage 2020). In summary, we adopt a similar formalism to that outlined in Crawford et al. (2010, hereafter C10), which describes a Bayesian approach to determining the intrinsic flux density of the brightest source within a given pixel. However, we marry the analytic approach of C10 with simulations to better account for our source selection function.

To debias the source flux densities of the catalogs presented in this work, three sets of simulations were generated: one set for 148 GHz selected sources and two sets for sources selected in the 218 GHz and MMF maps. Each simulation set is composed of a number of “trials,” and each trial corresponds to 1000 simulated sources injected into the filtered maps. In this way we straightforwardly capture the effects of noise and contamination in the data themselves. Care must be taken in constructing the simulations to ensure adequate statistics in the relevant regimes of flux density and spectral behavior to describe the source population.

To generate the simulations, we begin with the Fourier transform of a filtered point source centered on the survey map. We multiply this transform by the appropriate phase function to shift its location in angular space. We repeat this process and accumulate in Fourier space all the sources for the simulation. We then apply an inverse Fourier transform to produce a map (a “signal template”) with the simulated filtered sources (and nothing else). This template is then added to the filtered data. We developed this procedure as an efficient way to create signal templates with simulated sources located with subpixel accuracy.

For the 11 trials of 148 GHz simulations, flux densities were selected from a uniform random distribution ranging from 0 to 50 mJy. This range was chosen to extend below the completeness limit of the survey and up to a flux density at which we expect the completeness to be close to 1.0 and the debiasing to be small.

For the 18 trials of faint 218 GHz and MMF simulations, 218 GHz flux densities were selected from a random normal distribution with mean 10 mJy and standard deviation 5 mJy.²⁹ For MMF simulations, these were then assigned spectral indices randomly selected from a normal distribution with mean 3.4 and standard deviation 1.3, which are the parameters of the Gaussian that best fits the distribution of the DSFGs’ $\alpha_{148-218}$ values (listed in Table 4). The flux densities for 148 and 277 GHz were calculated from these, and each band’s simulated filtered sources were then added to the filtered data for that band. (As discussed in Section 4.1, 92% of MMF and 218 GHz selected sources are DSFGs, so this choice of spectral index distribution is appropriate.) For sources with measured

²⁹ As noted later in the text, the flux density distribution used for simulated sources is divided out in the final estimation of the likelihood function. The form of the distribution is chosen to provide enough statistical weight to simulate the ACT sample, but this choice does not impact the likelihood if chosen properly.

218 GHz flux density above 30 mJy, we used a set of nine trials of simulations populated uniformly in flux density in the range 0–100 mJy with spectral indices distributed according to the same Gaussian distribution used to debias the faint sample. For the MMF simulations, the maps for each of the bands were combined in the same way as outlined in Section 3.2. The full source recovery procedures (single band and MMF) were then performed on the associated trials, including the removal of Galactic contamination (Section 4.2).

As described in Sections 3.3 and 4.1, each source is identified as “selected” in the map (148 GHz, 218 GHz, or MMF) in which the source is detected with the highest S/N. Furthermore, for each source we identify a “primary band” for debiasing. In the case of 148 and 218 GHz selection, the primary band is simply the corresponding frequency band. For the MMF, however, there is no one-to-one correspondence with a frequency band. We therefore choose 218 GHz as the primary band for debiasing sources selected with the MMF, because this band has similar or better DSFG sensitivity compared to 277 GHz, and it has better calibration. This choice of primary band also makes the MMF-selected debiasing closer to the treatment for 218 GHz selected debiasing. Other bands are referred to as “secondary bands.” For instance, the secondary bands associated with MMF selection would be 148 and 277 GHz.

For primary-band debiasing, we use the simulations to estimate the likelihood function of the intrinsic flux density (S_1) of the brightest source in a resolution element, $\mathcal{L}(S_1) = P(S_1^m|S_1)$, where the superscript m indicates a measured quantity. This likelihood is corrected for the input flux distribution of the simulations. It captures the effects of the detector and confusion noise and selection process on the distribution of recovered flux density. We then multiply the likelihood by an analytic prior $P(S_1)$ that accounts for the expected distribution of source counts (Equation (2) of Gralla & Marriage 2020). This approach has the advantage of allowing changes to the analytic prior without the need for more simulations. The result is the primary-band flux density posterior $P(S_1|S_1^m) \propto \mathcal{L}(S_1)P(S_1)$. We report the median and 16% and 84% quantiles of this posterior as the primary-band debiased flux.

We take a simplified approach to multiband debiasing. As shown by C10 (Figure 2), debiasing of robust primary-band detections does not significantly benefit from information in other bands, particularly from noisier secondary bands. Therefore, we do not reestimate the primary-band debiasing in the multiband process, but use the primary-band posterior previously computed to constrain the secondary-band flux densities and associated spectral indices. In secondary-band debiasing, we use the low level of noise correlation between bands (Section 3.2) to decompose the two-dimensional likelihood into independent functions of S_1^m and S_2^m : $P(S_1^m, S_2^m|S_1, S_2) \approx P(S_1^m|S_1)P(S_2^m|S_2)$. For the MMF selection when the secondary band is 277 GHz, the secondary-band likelihood $P(S_2^m|S_2)$ is approximated as a Gaussian distribution centered on the simulated likelihood and with a width set by the error on the raw flux density. This is needed to capture the selection effects of the MMF. For all other selection method/secondary-band combinations, we simply approximate the likelihood as the Gaussian likelihood given the raw flux density and error. To formulate the prior, as in C10, we work in the parameter space of primary-band flux density and spectral index. We then factor the prior: $P(S_1, \alpha) = P(\alpha|S_1)P(S_1)$. The

conditional probability $P(\alpha|S_1)$ is the normalized sum of broad spectral index distributions for AGNs and DSFGs (Table 4, Row 8), weighted by the number of expected sources of each type, as established by count models for S_1 . $P(S_1)$ is the same analytic counts-based prior used in the primary-band debiasing. With these ingredients, we can construct the posterior distribution, also expressed in the (S_1, α) parameter space:

$$\begin{aligned} P(S_1, \alpha|S_1^m, S_2^m) &\propto P(S_1^m, S_2^m|S_1, \alpha)P(S_1, \alpha) \\ &\approx P(S_1^m|S_1)P(S_2^m|S_1, \alpha)P(\alpha|S_1)P(S_1) \\ &\propto P(S_2^m|S_1, \alpha)P(\alpha|S_1)P(S_1|S_1^m). \end{aligned} \quad (9)$$

The first line in Equation (9) is Bayes’s theorem. The second line expands the prior and assumes independent noise between flux densities to split the likelihood. The final line combines the S_1 likelihood and prior into the previously computed primary-band posterior distribution. This last line shows in practice how we implement the secondary-band debiasing. Equation (9) is transformed from the (S_1, α) parameter space to a function of S_2 according to $S_1/S_2 = (\nu_1/\nu_2)^\alpha$ and marginalized to obtain the posterior “debiased” distribution for S_2 . By marginalizing over S_1 , this method also produces a posterior distribution for α . We report the median and 16% and 84% quantiles of the debiased S_2 and α distributions.

Because the debiased secondary-band flux densities include a prior on the α distributions, in Appendix B we further investigate outliers in these distributions for which the debiased secondary-band flux densities could be less optimal. We do not find any evidence for an unusual source population altering the measured sample α distributions on which the priors are based.

4.3.2. Debiasing Applied to Catalogs

We apply these debiasing methods to the ACT catalogs. Figure 5 compares the debiased with the measured flux densities in each ACT band for AGNs (top row) and DSFGs, with both MMF selection (middle row) and 218 GHz selection (bottom row). We restrict the plotted population to sources with raw flux density less than 50 mJy, because above this flux level the debiasing has a minimal effect. The sources are categorized as AGNs or DSFGs according to their raw spectral indices as described in Section 5.1. For DSFGs, the primary debiasing band is 218 GHz. For AGNs, only 0 (6) of the 376 sources classified as AGNs were selected in 218 GHz (MMF) maps, so the vast majority of AGN-classified sources have 148 GHz as the primary debiasing band. (If we restrict to the 95% of AGNs selected at 148 GHz, there is no significant change to the plotted results.) The gray band in Figure 5 shows the standard error. Most shifts due to debiasing are at or within the standard error, the exception being DSFGs at 218 GHz and, to a lesser degree, AGNs and DSFGs at 277 GHz.

The primary effect of the debiasing in Figure 5 is a downshift (“deboosting”) in the distribution of flux densities. At the high flux density end, this effect increases with decreasing flux density as the prior based on source counts becomes more important. At the lowest flux densities, the debiasing of AGNs and of 218 GHz selected DSFGs behaves differently from MMF-selected DSFG debiasing. For the former, in the primary band (148 GHz for AGNs, 218 GHz for DSFGs), the deboosting continues to the lowest fluxes. In the secondary bands at low fluxes, the imposition of an α prior in conjunction with the robust primary-band detection counters

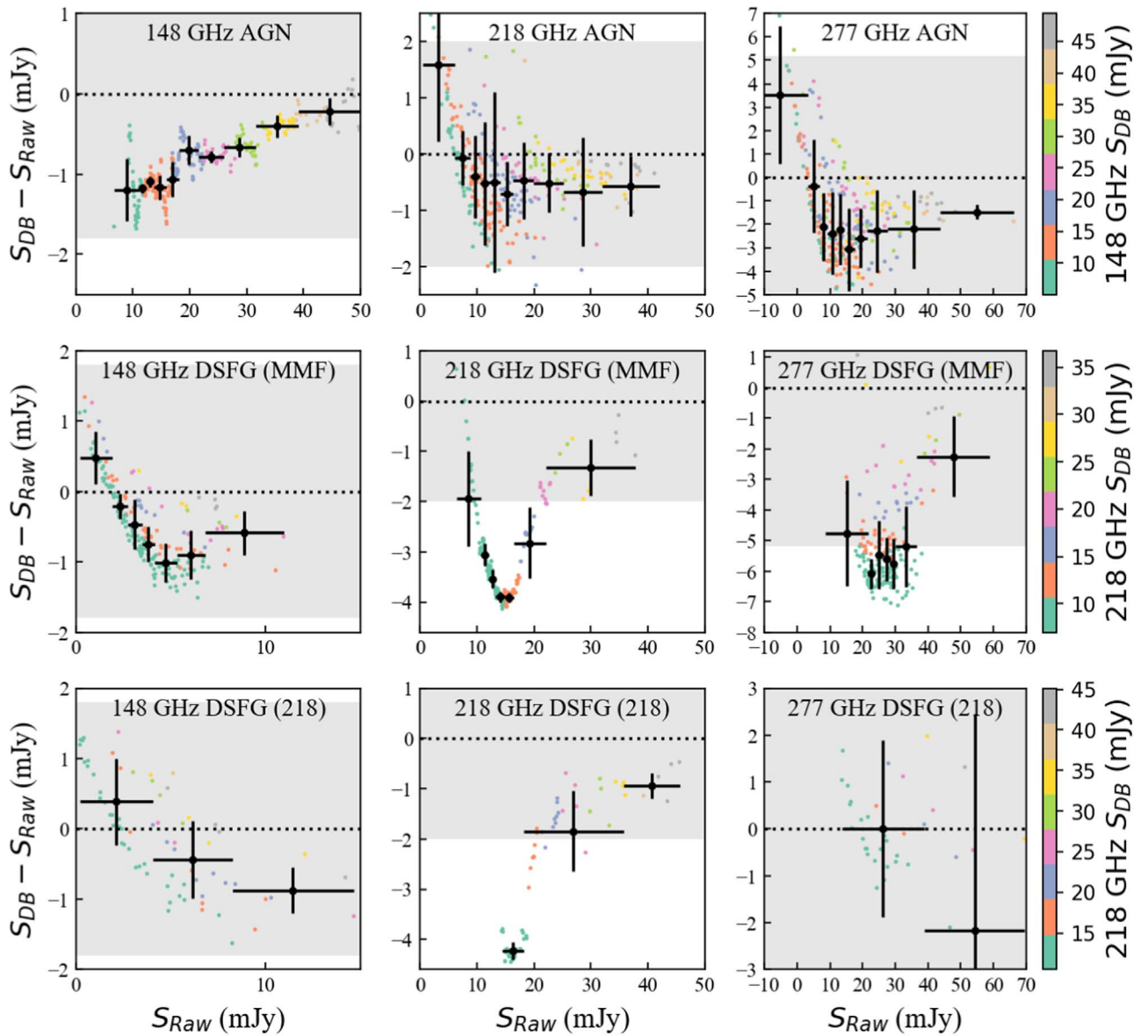


Figure 5. Debiased flux densities vs. measured flux densities in each ACT band for sources in the extragalactic catalog. The top row shows debiasing for AGNs, of which 95% are selected at 148 GHz. The other panels are for DSFGs, which are selected with the MMF (middle row) or 218 GHz data (bottom row). In these panels, the debiased flux density minus the raw flux density is shown on the y-axis. Points, color-coded by primary-band flux density, show results for individual sources, while the black data with errors show the mean and standard deviation on these points in bins of width indicated by the horizontal bars. Except for the highest flux density bins, each bin is chosen to contain 30 sources. The light-gray region indicates the characteristic statistical uncertainty associated with each band, centered at zero (in some cases extending beyond the plotted y-axis limits). For top and bottom rows, not all sources have corresponding 277 GHz data. The debiasing shifts the flux densities downward to correct for Eddington bias (i.e., “deboosting”). This behavior is altered at the lowest flux densities owing to interband information communicated through the likelihood and priors.

the deboosting effect. As the measured flux density in the secondary band reaches zero (or even negative values), this results in a positive correction. Also, additional scatter is seen in the secondary-band debiasing plots. This is expected owing to the combination of noise and the imposition of independent information from the primary band through the α prior.

For DSFGs selected with the MMF, even in the primary 218 GHz band, the debiasing diminishes below 15 mJy. All DSFGs in this flux density range are below the 218 GHz 5σ detection threshold and so *require* the MMF selection, which has a significant contribution from the 277 GHz data. The simulated MMF likelihood captures the probability that a source with S_{218}^m below the 218 GHz detection threshold has

higher intrinsic S_{218} given the extra information from the 277 GHz band. This is also an effect for the 277 GHz band, which inflects below its nominal threshold of ~ 30 mJy. In contrast, the story is simpler for the subthreshold 148 GHz data, which are debiased through the α prior, similar to the secondary bands for the AGNs.

Because the 277 GHz band plays an important (albeit high noise) role in the MMF, we take one more step to estimate the intrinsic 277 GHz flux density. Sources below the 218 GHz detection limit (< 15 mJy) are only detected if they have a correspondingly strong 277 GHz flux density measurement. This introduces a selection effect whereby, at low 218 GHz flux density, the MMF is biased toward selecting sources with

measured 277 GHz flux density scattered high. As noted in Section 4.3.1, we use the simulations to centroid the 277 GHz likelihood function for MMF-selected DSFGs, analogous to the first step of the primary-band debiasing. The resulting 277 GHz flux density posterior thus captures this selection effect and includes a modest, extra debiasing contribution from this simulated likelihood. This illustrates how the use of simulations can capture subtle selection effects introduced by use of nontrivial data filters.

When implementing these methods, one must select an angular separation tolerance with which to match the measured positions of recovered simulated sources with the input positions. If this tolerance radius is too small, sources that should be matched will be missed, and the statistics of the simulated catalogs will suffer and possibly be biased toward brighter sources. If this tolerance radius is too large, spurious matches can be introduced. Because the primary-band flux density prior, which is derived primarily from the source counts, is so steep with so much power at low flux densities, spurious matches seen as low outliers in the likelihood function become greatly exaggerated in the resulting posterior distribution. For each set of simulations, the tolerance radius is initially chosen based on inspection of the distribution of distances between the input and measured positions for sources matched with an initially very large radius. After matching using a tolerance radius thus determined, we then also remove sources that appear to be recovered but have input flux densities well below the completeness limit of the survey. Finally, in a plot of the measured versus debiased flux densities, sharp discontinuities occur where misidentified simulated sources bring the debiased flux densities erroneously low. We verify that the primary-band debiased flux density is a smoothly varying function of the measured flux density for each selection, as is evident in the top left and central lower two panels of Figure 5. For the MMF selection, we use a tolerance radius of $0''.005$ ($18''$) and remove matched sources with input flux density below 4 mJy (below which we are unlikely to recover simulated sources that are true rather than spurious matches; e.g., see the completeness in Figure 6). For the 218 GHz selection, we use a tolerance radius of $0''.007$ ($25''.2$) and remove matched sources with input flux density below 4 mJy. For the 148 GHz selection, we use a tolerance radius of $0''.004$ ($14''.4$) and remove matched sources with input flux density below 6.5 mJy. We calculate the debiasing correction for sources selected at 148 GHz up to 50 mJy. Above these limits, the debiasing becomes very small, and our simulations do not include enough bright sources to robustly determine the debiasing. All MMF and 218 GHz selected sources are debiased.

4.3.3. Completeness

These simulations also provide an estimate of the sample completeness as a function of intrinsic flux density. We calculate the numbers of simulated sources that are matched to sources recovered from the source-finding procedure. The completeness is given by the ratio of the number recovered to the number input for the 148 GHz, MMF, and 218 GHz selections. For each of these selection methods we recast the completeness in each band as a function of the flux density in that band. The results are shown in Figure 6. For 218 GHz and MMF-selected samples (which are 92% DSFGs), we restrict the simulated sources to those with input $\alpha > 1.0$ to mimic our

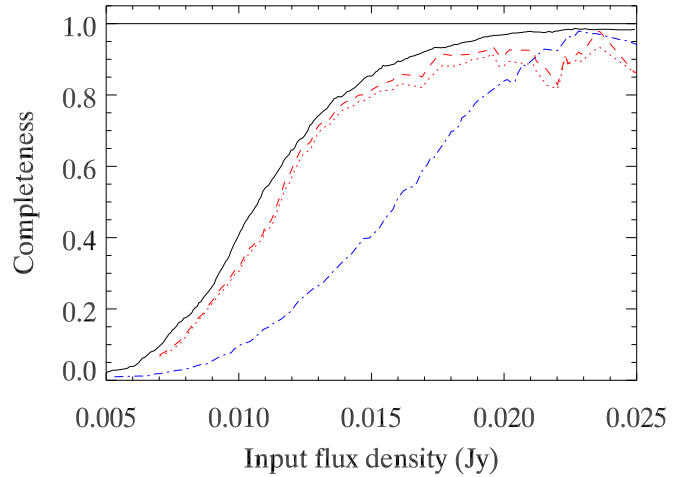


Figure 6. Completeness as a function of flux density, as determined by recovering simulated sources. The black solid curve represents the 148 GHz selection, shown as a function of input 148 GHz flux density. The red dashed (dotted) curves represent the MMF selection before (after) the Galactic dust cuts have been applied. The blue dotted-dashed curve represents the 218 GHz selection, after the dust cuts have been applied. For the MMF sample, the completeness is shown as a function of primary-band 218 GHz flux density. The 148 GHz, MMF, and 218 GHz selected samples are 50% complete at 10.5, 11.5, and 16 mJy, respectively.

DSFG selection criterion. In this way, the MMF and 218 GHz selection completeness is equivalent to the completeness of DSFG selection, a fact we use when estimating DSFG source counts. We also apply the same cuts to remove Galactic dust (described in Section 4.2) from the simulated source samples. Figure 6 shows the MMF completeness with and without these dust cuts, which do not strongly affect the completeness of extragalactic DSFGs. The MMF completeness never reaches 100% even without Galactic cuts because of our criterion that the input α be greater than 1.0, which excludes 3.2% of the population (see Figure 12 for the α distribution). We do not need to impose a similar criterion on the AGN simulations because the distribution in α is much narrower, and the resulting cut would only exclude 0.007% of the population. In the same way as we equate 218 GHz and MMF completeness to that of DSFGs, the AGN completeness, used for source count estimation, is taken to be the same as 148 GHz completeness. This association is reasonable, as 95% of AGNs are selected at 148 GHz.

We made one modification to the simulated source sample when calculating the 148 GHz flux density sample completeness. In our main source-finding pipeline, sources that are located within $25'$ of very bright ($S/N > 50$) sources are excluded from the sample. However, because there are many such bright sources in the simulated samples, given the input distribution of S_{218} and $\alpha_{148-218}$, this practice excludes a nonnegligible ($\sim 10\%$) fraction of the catalog. We ran a separate source-finding trial on one of the 1000-sample simulated source maps, reducing the size of the exclusion region to $1'$, and the completeness curve is based on this trial rather than the full sample. This exclusion would not affect the main catalogs because we first mask any bright sources and rerun the source finding after they have been removed. Shrinking the exclusion region to $1'$ does not affect the filter for the simulations because we construct the filter from the

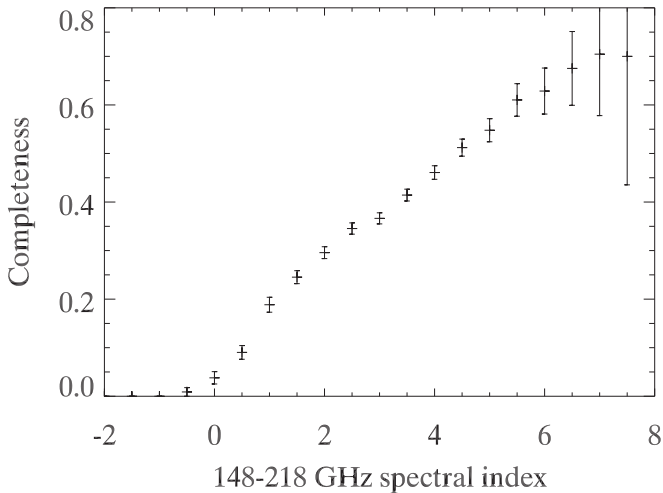


Figure 7. MMF completeness as a function of spectral index, as determined by recovering simulated sources. Note that the DSFG sample is selected using the criterion $\alpha_{148-218} > 1.0$, so DSFGs with shallower, flat, or negative spectral indices would be classified as AGNs and removed from the DSFG sample.

maps of the real data, so the filter does not include noise from the simulated sources.

The MMF completeness depends on the spectral index, as well as the flux density. We use the same set of MMF simulations to investigate this dependence, shown in Figure 7. We populated the MMF simulations with an input α distribution that is Gaussian with mean 3.4 and standard deviation 1.3 to approximate a DSFG source population. The uncertainty on the completeness reflects this, as the completeness is better determined for the more numerous simulated sources with α near the center of the input distribution. Note that the completeness in Figure 7 never approaches unity because, for each bin in α , it is computed over the full population of sources. With mean $S_{218} = 10$ mJy and standard deviation 5 mJy, this population includes many sources well below the detection threshold.

4.4. Purity

To calculate the catalog purity, we multiplied the maps by -1 and ran our source-finding algorithms. For the 148 GHz map, the Sunyaev-Zel’dovich (SZ) effect associated with galaxy clusters introduces compact negative signals in the map (which become compact positive signals after multiplication by -1). We therefore masked out $6'$ regions around the optically confirmed galaxy clusters presented in Hasselfield et al. (2013a). Bright sources also introduce negative (i.e., positive after multiplication by -1) features nearby owing to ringing from the filtering. We generated a template of the sources by populating a map with the beam profile at the position and amplitude of each source in the catalog, and we subtracted this template from the 148 GHz map before inverting it. Three sources (10–17 mJy) are detected in the inverted map, after disregarding the few detections near bright features. Thus, according to this analysis, the estimated departure from purity in the AGN sample is at the $(3/376) < 1\%$ level. For comparison, based on simulations of the noise in the map, Hasselfield et al. (2013a) expected 1.8 false positives.

For the sources selected via the MMF, we first inverted the multiband map and ran the source-finding algorithm. We then applied the cuts to eliminate Galactic dust emission, which may

Table 3
Astrometry

	N_{match}^a	R.A. ^b		Decl.	
		Mean	σ	Mean	σ
148 GHz, S/N > 5	264	−0.02	5	−0.8	5
148 GHz, S/N > 16	94	−0.2	2	0.1	2
MMF, S/N > 5	151	−0.1	4	−2	5
MMF, S/N > 16	47	−0.1	2	−0.8	2

Notes.

^a ACT locations are compared to matched FIRST source locations, which have $0''.5$ precision.

^b Offsets listed in arcsec.

also introduce negative sources into the map through ringing from the filter. After applying Galactic cuts and again removing sources near bright features, only one source (13 mJy) is recovered from the inverted map. Thus, the estimated departure from purity in the MMF-selected DSFG sample is at the $(1/200) < 1\%$ level.

For sources selected at 218 GHz outside the area of the MMF map, we also inverted the map, ran the source-finding algorithm, and applied the Galactic dust cuts. Because most of this area lacks reliable 277 GHz data, we did not cut based on source spectrum. The dust cuts reduced the number of sources found in the inverted map (after removing a few near bright features in the map) from 85 to 7. Of these, five are clearly associated with extended Galactic dust emission. According to this analysis, the estimated departure from purity in the 218-selected DSFG sample is at the $(2/68) < 4\%$ level.

We note that the map-inversion method described here does not account for false detections due to Galactic dust contamination. We have taken careful measures to remove such contamination (Section 4.2). Using source counts, we further check that the catalog is not significantly biased by Galactic dust contamination. This check is described in Section 5.2.1 (Figure 14).

4.5. Astrometry

To determine the accuracy of the catalog astrometry, we matched ACT sources within $1/2$ of radio sources selected from the VLA FIRST survey (Becker et al. 1995). The positional uncertainty for FIRST sources with 1.4 GHz flux densities above 3 mJy is $< 0''.5$. For a summary of the astrometric offsets, see Table 3. For the 148 GHz catalog, there are 268 ACT sources with matches in FIRST, 264 of which have integrated 1.4 GHz flux density > 3 mJy. The mean difference in R.A. between the ACT sources and the FIRST sources is $-0''.02$, and the standard deviation of this difference is $5''$. The mean difference in decl. between the ACT sources and the FIRST sources is $-0''.8$, and the standard deviation of this difference is $5''$. Because the FIRST survey has a high angular resolution ($5''$), some extended radio sources may be resolved into multiple components. If we restrict the matched sample to ACT sources that only have a single FIRST match, there are 204 matches and the positional differences do not change qualitatively. If we restrict the sample to ACT sources that have S/N above 16, there are 94 matches. Figure 8 shows the results of this matching. For this sample, the mean difference in R.A. between the ACT sources and the FIRST sources is $-0''.2$, and the standard deviation of this difference is

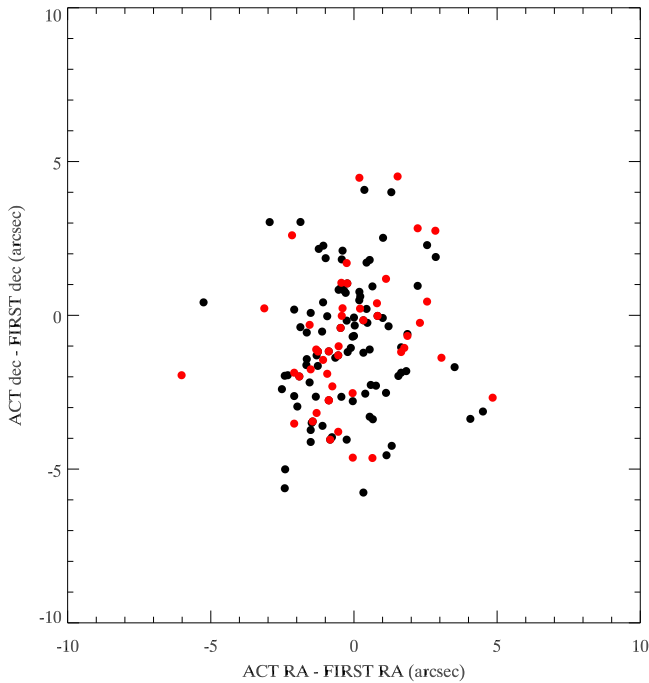


Figure 8. Positions of ACT sources with $S/N > 16$ relative to FIRST positions. Black points represent locations from the 148 GHz data, and red points represent locations from the MMF data.

$2''$. The mean difference in decl. between the $S/N > 16$ ACT sources and the FIRST sources is $0''.1$, and the standard deviation of this difference is $2''$.

The angular resolution of the 218 GHz map is higher, although the noise level is also higher. If we adopt the 218 GHz positions of the 148 GHz selected sources, there are fewer matches to FIRST sources (218) and the scatter between the ACT and FIRST positions is higher ($6''$). This is likely due to the higher significance of the 148 GHz measurements, which are both more sensitive and in a brighter part of the typical SED for AGNs. For the 40 sources with 218 GHz $S/N > 16$, the scatter between the 218 GHz positions and the FIRST positions is reduced to $2''$ – $3''$.

For sources selected through the MMF technique, there are 151 with matches in the FIRST catalog (after the dust cuts are applied to the ACT sample, which removes two sources). The mean difference in R.A. between the ACT sources and the FIRST sources is $-0''.1$, and the standard deviation of this difference is $4''$. The mean difference in decl. between the ACT sources and the FIRST sources is $-2''$, and the standard deviation of this difference is $5''$. For the 47 sources with $S/N > 16$ and FIRST matches, the scatter between the ACT positions and the FIRST positions is reduced to $2''$ in R.A. and $2''$ in decl.

We can compare the astrometric accuracy with previous ACT source analyses. Marriage et al. (2011) matched ACT sources from the southern survey having $S/N > 20$ with AT20G sources and found the rms of the offsets to be $3''.5$ in R.A. and $3''.3$ in decl. For sources with $S/N > 16$, Marsden et al. (2014) found the rms of the offsets to be $2''.1$ in R.A. and $1''.8$ in decl. at 148 GHz (and larger, $\sim 3''.5$ at 218 GHz). Thus, the astrometry of the ACT equatorial source catalog is comparable to earlier ACT source catalogs. This is as expected, because the instrument beam did not change significantly between the

southern and equatorial surveys, and similar S/N thresholds were considered.

5. Source Characterization

5.1. Millimeter Spectral Indices

The spectral behavior of sources across the ACT bands is bimodal owing to the presence of two distinct populations: AGNs and DSFGs. Table 4 summarizes the typical spectral indices for these source populations, as discussed throughout this section, which is organized as follows. First, we discuss the spectral properties of all the sources in the catalogs as measured by ACT. We then split the sample into the two dominant populations and report the sample statistics for each. We next describe tests of our recovery of spectral information, and last we discuss our results and compare with other studies. Sources that are flagged as Galactic (see Section 4.2) are not included in the following analyses or figures.

5.1.1. Spectral Properties of the Full Sample

Figure 9 plots 148 GHz flux density versus 218 GHz flux density, and Figure 10 plots 218 GHz flux density versus 277 GHz flux density for all sources in the catalog. The DSFG sample populates the higher spectral indices and mostly lower flux densities (and many are undetectable at 148 GHz), while the AGNs extend to higher flux densities. Both the raw measured and debiased (Section 4.3) flux densities are shown. The debiasing methods tend to concentrate the sources into the two populations, as expected for the lower significance data given the prior probability distribution (see Figure 11).

Figure 11 plots the 148–218 GHz spectral indices versus the 218–277 GHz spectral indices. The two populations are clearly discernible, and the 218–277 GHz spectral indices are flatter (closer to 0) than the 148–218 GHz spectral indices for the DSFGs. Spectral indices plotted in Figure 11 are estimated directly from flux densities as $\alpha = \log(S_2/S_1) / \log(\nu_2/\nu_1)$. The black points show indices estimated from raw flux densities, while those computed from debiased flux densities are shown in red. Note that these spectral indices derived from debiased flux densities are not exactly the same as what is reported in Table 4; in the latter, spectral indices are calculated directly from a posterior computed from Equation (9). Indeed, for AGNs, we do not even compute the 218–277 GHz spectral index through the posterior. The sources that have been visually identified in SDSS optical images as nearby dusty galaxies are shown in blue. Although they lie within the DSFG spectral index distribution, their $\alpha_{218-277}$ typically falls on the flatter side of the distribution, as also seen in the sample medians reported in Table 4. This could be explained by sources that are extended and thus resolved in the 277 GHz maps or by CO line emission at 230.5 GHz contributing to the 218 GHz flux densities. In Appendix B we further investigate the sources with spectral indices that lie at the edges of the distributions.

Figure 12 shows a histogram of the measured 148–218 GHz spectral indices. As seen in the figure, the two populations are clearly distinguishable. The flux densities used to construct this histogram have not been debiased. A simple model consisting of two Gaussians, one describing each population, has been fit to the data and is also shown. The best-fit median spectral index for the AGNs is -0.8 , with standard deviation 0.4. The

Table 4
Typical Millimeter Spectral Indices for AGNs and DSFGs

Median Spectral Indices	AGNs				DSFGs			
	Median α_{148}^{218}	σ	Median α_{148}^{277}	σ	Median α_{148}^{218}	σ	Median α_{218}^{277}	σ
Full sample ^a	-0.66	1.2	-0.54	1.9	3.7	1.8	2.4	4.2
Restricted to $-1^\circ 2 < \text{decl.} < 1^\circ 2$	-0.65	0.9	-0.45	1.1	3.6	1.6	2.7	1.5
Restricted to $S > 20$ mJy AGNs	-0.62	0.67	-0.50	1.0				
Restricted to $S > 50$ mJy AGNs	-0.58	0.32	-0.49	1.3				
Bootstrap samples ^b	-0.66	0.03	-0.54	0.04	3.7	0.13	2.4	0.11
Debiased spectral indices ^c	-0.52	0.6	-0.67	2.6	3.8	1.1	2.8	1.1
Parameters describing best-fit Gaussian	-0.8	0.4			3.4	1.3		
Prior used in debiasing secondary bands	-0.7	1.2	-0.4	3.4	3.7	2.2	2.7	2.1
Nearby dusty galaxies					4.0	1.7	1.3	4.2

Notes.

^a The spectral indices reported here are based on raw (not debiased) flux densities, except where otherwise noted.

^b For this row, σ denotes the standard deviation of the medians, while for the other rows σ denotes the sample standard deviation. The statistics reported here are based on resampling the full catalog 1000 times.

^c The debiased spectral index for each source is calculated from the posterior distribution of the spectral index, as discussed in Section 4.3. For α_{148}^{277} and α_{218}^{277} , the sources are restricted to $-1^\circ 2 < \text{decl.} < 1^\circ 2$.

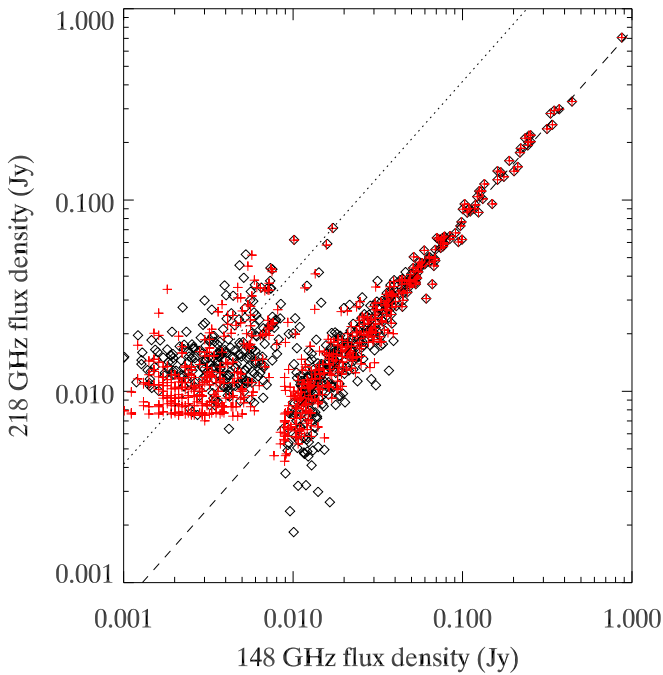


Figure 9. 148 GHz flux density vs. 218 GHz flux density. Black diamonds (red plus signs) are raw (debiased) flux densities. The dashed line indicates the best-fit median AGN spectral index (-0.8), and the dotted line indicates the best-fit median DSFG spectral index (3.4). The population at the right extending to higher flux densities is composed of AGNs, whereas the fainter, 218 GHz dominated population is composed of DSFGs.

best-fit median spectral index for the DSFGs is 3.4 , with standard deviation 1.3 . These values are listed in Table 4.

5.1.2. Spectral Properties of AGN and DSFG Populations

We split the sample into AGNs and DSFGs according to their measured (not debiased) 148–218 GHz spectral indices. Sources with $\alpha > 1.0$ are identified as DSFGs, and sources with $\alpha < 1.0$ are identified as AGNs. Because the populations are less easily separated by the 218–277 GHz spectral indices (Figure 11), we identify every source as an AGN or DSFG based solely on its 148–218 GHz spectral index. As listed in

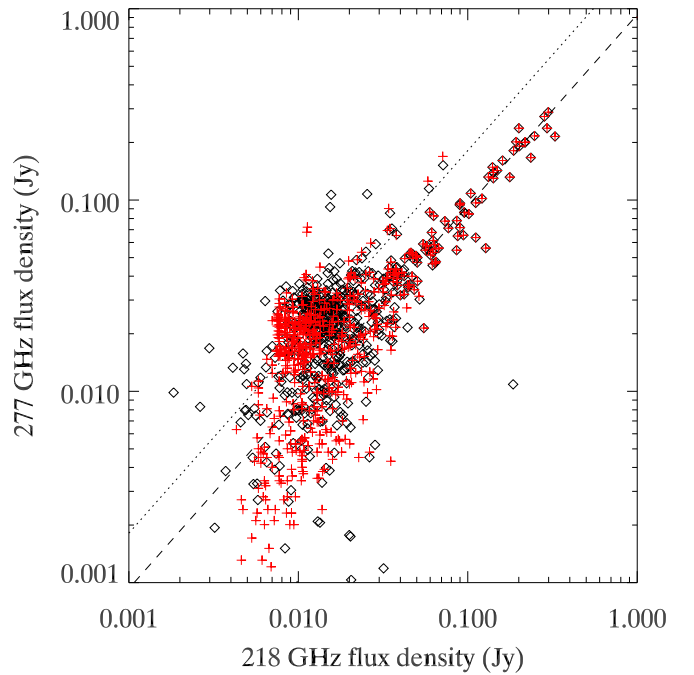


Figure 10. 218 GHz flux density vs. 277 GHz flux density. The plotting convention is the same as in Figure 9. The dashed line indicates the median AGN spectral index (-0.33), and the dotted line indicates the median DSFG spectral index (2.4). The AGN and DSFG populations are no longer clearly distinguishable. The MMF allows us to detect DSFGs below the typical 218 GHz 5σ noise threshold.

Table 2, 376 sources are classified as AGNs, and 268 sources are classified as DSFGs. In Appendix B, we further investigate the sources with spectral indices that fall near the AGN/DSFG boundary.

The median spectral index for AGNs is -0.66 for 148–218 GHz and -0.54 for 148–277 GHz, as shown in Table 4. The median spectral index for DSFGs is 3.7 for 148–218 GHz and 2.4 for 218–277 GHz. The sample standard deviations are also reported in Table 4. The medians and standard deviations of the debiased spectral indices, as derived from the debiasing analysis summarized in Section 4.3, are also

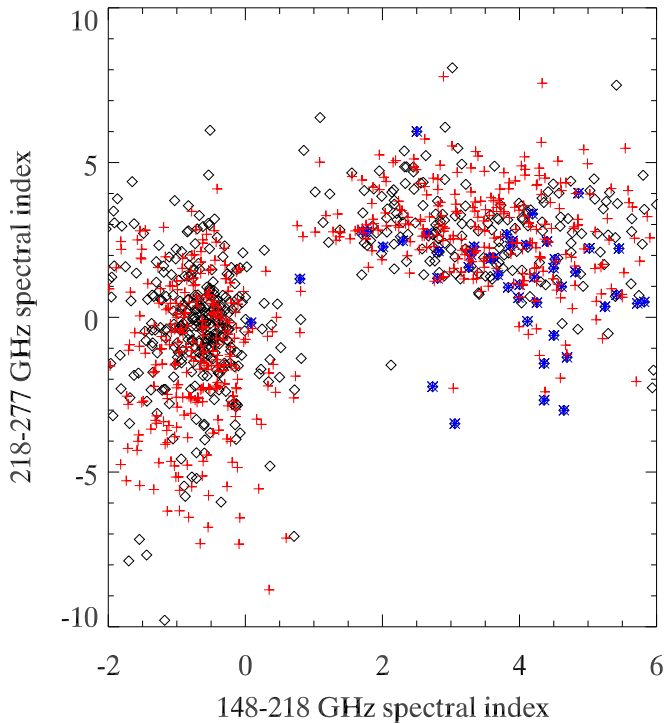


Figure 11. Color-color diagram of all sources. Black diamonds (red plus signs) are raw (debiased) spectral indices. The blue stars are nearby dusty galaxies. The DSFG (at right) and AGN (at left) populations clearly separate. As expected, this separation is even more pronounced for the debiased flux densities.

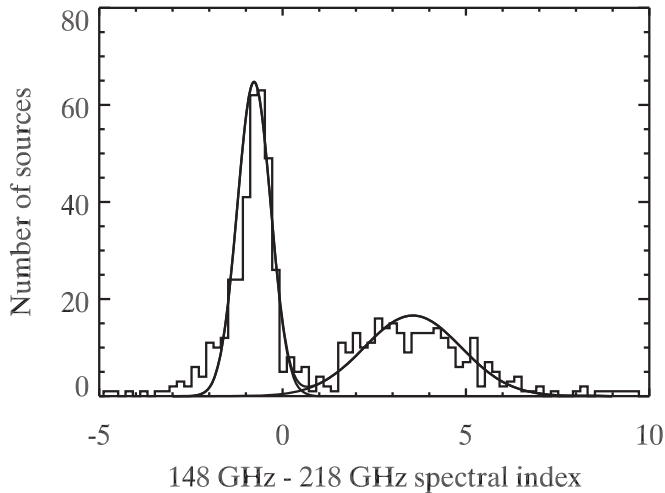


Figure 12. Histogram of the spectral index α from 148 GHz to 218 GHz ($S \propto \nu^\alpha$). The two source populations, AGNs and DSFGs, are discernible. A model composed of two Gaussians, one for AGNs and one for DSFGs, is fit to the data and overplotted, with best-fit model parameters listed in Table 4.

presented in Table 4. In order to estimate the uncertainty on the medians, we randomly select sources from the sample to generate bootstrapped catalogs. The median and standard deviations on the medians for 1000 such catalogs are reported in the line for “Bootstrap samples” in Table 4.

We compare the distributions of 148–218 GHz spectral indices with the distributions of spectral indices involving 277 GHz for both AGNs and DSFGs. For AGNs, the median measured α for 148–277 GHz is -0.54 , compared to -0.66 for 148–218 GHz. However, debiasing the flux densities affects the AGN

148–277 GHz α more, such that the debiased 148–277 GHz α is steeper (-0.67 if restricted to the MMF area) than both the measured 148–277 GHz α and the debiased 148–218 GHz α . For DSFGs, the median 218–277 GHz spectral index is flatter (closer to 0) than the median 148–218 GHz spectral index. The median measured α for 218–277 GHz is 2.4 for DSFGs (2.7 if restricted to the MMF area, 2.8 for the debiased spectral indices), compared to 3.7 for 148–218 GHz (3.8 for the debiased spectral indices), which we interpret as evidence for optically thick emission near the peak of the thermal spectrum or an additional cold dust component (see Section 5.1.4).

The increased scatter for spectral indices involving the 277 GHz band can be explained by the higher noise level at 277 GHz. For example, for a high-S/N source with $S_{148} = 15$ mJy, a spectral index of -1 results in $S_{277} = 8$ mJy. Typical noise at 277 GHz is 5.2 mJy. Thus, $\pm 1\sigma$ on the 8 mJy translates to an apparent range in the 148–277 GHz spectral index of -2.7 to -0.2 . For both populations, the standard deviation of spectral indices involving 277 GHz is reduced when we constrain the sample to sources in an area of the map with lower noise in the 277 GHz data.

5.1.3. Tests of Spectral Index Recovery

Using mock catalogs, we find that noise in the 277 GHz data does not account for the flatter 218–277 GHz spectral index for the DSFGs, but it does account for the flatter measured spectral index for the AGNs. The mock catalogs are generated as follows. For every source, we assign a mock 277 GHz flux density by scaling the 218 GHz flux density to 277 GHz assuming the 148–218 GHz spectral index measured for that source. We add normally distributed noise with width equal to the 277 GHz measurement error for that source, repeat this mock 277 GHz flux density generation over the entire catalog, and then repeat this analysis to generate 1000 catalogs. Of these 1000 catalogs, none return a median 218–277 GHz spectral index as flat as the measured median 218–277 GHz spectral index for the DSFGs. For these mock catalogs, the median 148–277 GHz spectral index is -0.55 for AGNs (-0.44 when restricted in decl. to $-1^\circ 2 < \text{dec} < 1^\circ 2$), which agrees well with the median measured 148–277 GHz spectral index. Thus, the mock AGN 148–277 GHz spectral index is measured to be shallower than the input in a way that reproduces what is observed. For DSFGs, the median 218–277 GHz spectral index of the mock samples is 3.4, which is steeper than the median measured 218–277 GHz spectral index of the catalog (2.4, or 2.7 when restricted in decl.).

5.1.4. Discussion of Spectral Indices

We interpret the flattening of the dust spectrum from 218 to 277 GHz as indicating that a nonnegligible optical depth is likely introducing curvature to the spectrum. Alternatively, emission models that include a cold dust component (e.g., two-temperature models such as Dunne & Eales 2001) may also be able to reproduce the spectral flattening that we observe at the higher ACT frequencies. However, without more observations at other frequencies, it is difficult to distinguish between optically thin dust emission at different temperatures and optically thick emission models. We note that our use of α to describe the dust spectrum from 218 to 277 GHz is only a convenient parameterization rather than a description of a true underlying power-law spectrum. Su et al. (2017) combine the

ACT data with flux densities from *Herschel* and model the SEDs of a subset of nine of the DSFGs in our sample (as further discussed in Section 6). The best-fit models indicate that the spectra become optically thick at higher frequencies. This introduces a factor of $1 - e^{-\tau}$ into the spectrum (see Equations (3)–(5) in Su et al. 2017). The median 148–218 GHz α and the median 218–277 GHz α of the subsample presented in Su et al. (2017) are 3.5 and 2.6, respectively. These agree with the median values of α for the full DSFG sample. Given that these sources are likely strongly lensed, it is not surprising that their SEDs are representative of their fainter counterparts in the full DSFG sample.³⁰ For nearby ($z < 0.09$) dusty galaxies, even flatter 218–277 GHz spectral indices (and steeper 148–218 GHz spectral indices) are likely due to contamination by CO $J(2-1)$ line emission. High-redshift galaxies are not similarly contaminated by this CO line because it is redshifted out of the ACT 218 GHz band. In Gralla et al. (2014), we stacked ACT and *Herschel* data for radio-selected nearby star-forming galaxies and modeled their median SEDs. Our best-fit model contained a 2.8 mJy contribution to the 218 GHz flux densities from CO line emission. This was found to be in agreement with an example star-forming galaxy. To investigate the potential contribution of CO to the SEDs of nearby galaxies in this sample, we subtract 2.8 mJy from their measured 218 GHz flux densities. This brings the median 148–218 GHz α for the nearby galaxies (4.0 before subtracting, 3.7 after) into agreement with the full sample (3.7). Similarly, subtracting the 2.8 mJy brings the nearby galaxies’ 218–277 GHz α (1.9 before subtracting, 2.6 after) into agreement with the full sample (2.7).

For the AGNs, to compare our spectral index results with previous studies, we restrict our sample to match these studies’ flux density limits. If we restrict the sample to sources whose 148 and 218 GHz flux densities both exceed 20 mJy (50 mJy), then the best-fit median spectral index for the AGN is -0.62 (-0.58). For comparison, the median α for sources with $S_{148} > 50$ mJy in Marsden et al. (2014) is -0.6 . However, the median α for fainter sources in Marsden et al. (2014) (-0.51) is shallower than for $S < 50$ mJy sources in this sample (-0.7), at low (2σ) significance. Mocanu et al. (2013) also find that the fainter AGNs in their sample have relatively steeper spectral indices.

5.2. Source Counts

5.2.1. Description of Source Counts

The differential source number counts for each ACT band and for each subpopulation (AGNs and DSFGs) are shown in Figure 13 and listed in Table 5. The sources have been classified as AGNs if their spectral index from 148 to 218 GHz (based on the measured flux densities, not the debiased flux densities) is less than 1 and as DSFGs if this spectral index is greater than 1, as discussed in Section 5.1. For 148 GHz sources below 90 mJy and for all MMF-selected sources, the source counts are constructed using full posterior distributions (as described in detail below) of the debiased flux densities (when available, for sources with $S_{148} > 50$ mJy the measured

flux densities are used). Above 90 mJy for the 148 GHz AGN counts, we use all the available survey area (949 deg²). Below 90 mJy, we restrict the 148 GHz AGN counts to the 505 deg² in the main survey field (Figure 1). We further restrict the DSFG counts to the MMF selection and map, which is 277.2 deg².

The source counts are corrected for incompleteness in the following manner. For a given source in the catalog, we select sources from the simulations described in Section 4.3 that have similar input flux densities. The tolerance used is the median 1σ error on the source flux densities for the band and source category (AGN/DSFG) under consideration. For the set of simulated sources, we compute the fraction that are recovered ($f_{r,i}$). When computing the source counts, we weigh each i th source by $1/f_{r,i}$.

The debiasing method provides posterior probability distributions for the intrinsic flux densities of all the sources in the catalogs. These full distributions should be taken into account when calculating the number counts from the debiased flux densities. In the case of the DSFGs, which have very steep source counts, using only the median debiased flux densities instead of the full probability distributions would introduce both a bias and scatter in the counts.

To bring the full posterior probability distributions of the source flux densities into the source counts computation, we calculate the source counts using mock catalogs generated in the following way (similar to what is done in Coppin et al. 2006; Austermann et al. 2009; Mocanu et al. 2013). We make a list of mock flux densities by varying the debiased flux densities around their (asymmetric) errors. For AGNs with $S_{148} > 50$ mJy, for which debiased flux densities are not calculated, we vary the measured flux densities around their raw measurement errors. We generate a list that is 1000 times the catalog sample size, calculating the completeness for every source by interpolating the completeness versus flux density to the value for each of these flux densities. We then generate 1000 mock samples, drawing from this flux density list. The size of each mock sample is drawn from a normal distribution with mean equal to the size of the catalog and error equal to the square root of the size of the catalog. Sources are permitted to fall below the 8 mJy threshold of the lowest flux density bin, so in practice the mock samples are smaller than the catalog. We calculate the source counts for these 1000 trials. For each flux density bin (excluding AGNs with $S_{148} > 90$ mJy), the source counts shown in Figure 13 and reported in Table 5 are the median source counts across these trials. The errors are calculated from the 16th and 84th percentiles of the distribution of the source counts from the trials, which are generally in agreement with the median of the Poisson, completeness-corrected errors. The value used as the central flux density for each bin is the median (across all mock catalogs) of the median (across all sources within the bin for each mock catalog) flux densities. This procedure, based on the debiased flux densities, naturally corrects for sources that should lie below the lowest flux density bin being boosted into the catalog by noise.

Finally, there is an overall calibration uncertainty (as discussed in Section 2) that also applies to the source counts. The uncertainty this introduces on the source counts is relatively small and is represented by the horizontal error bars in Figure 13.

One way our approach differs from the previous analyses that compute source counts in this way (Coppin et al. 2006;

³⁰ Alternatively, one could expect that the lensed sources might be drawn from a higher-redshift population. In the submillimeter wavelengths at these bright flux densities, and given the high-redshift nature of most unlensed submillimeter galaxies, the redshift distribution is actually expected to be similar between the lensed and unlensed populations (e.g., Hezaveh & Holder 2011).

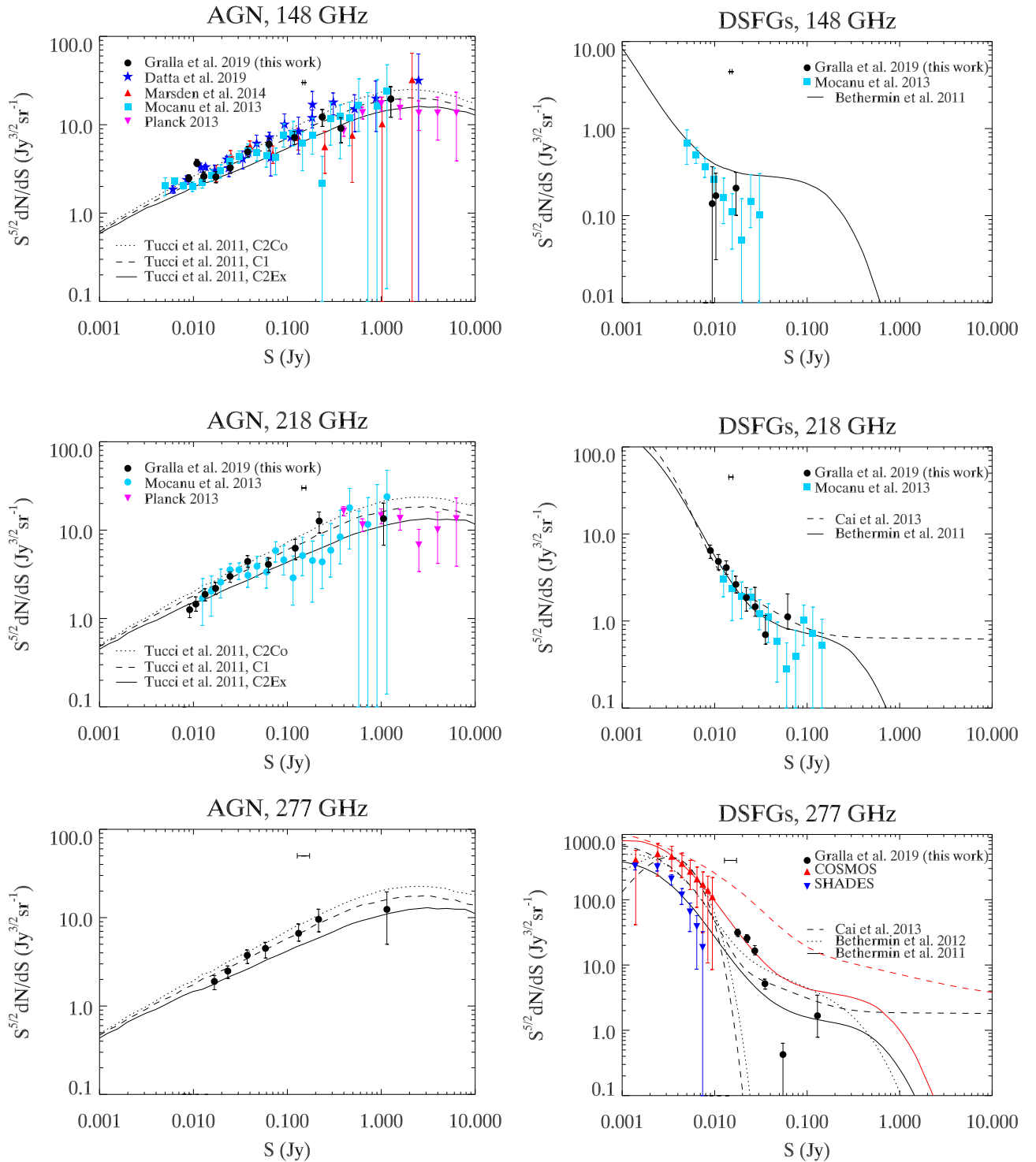


Figure 13. Source number counts for the ACT AGN and DSFG source samples. Black circles represent the source counts of the catalog presented in this paper, calculated by sampling the posterior distributions of the debiased flux densities (as described in Section 5.2) for all but the bright ($S > 90$ mJy) AGNs, which are calculated directly from the catalogs. Other data sets and models are presented as labeled in the legends. A horizontal black error bar at the top of each plot indicates the band-dependent calibration uncertainty. In all plots, the counts have been corrected for completeness, values for which are listed in Table 5 for each flux density bin. On the left, AGN source counts are shown in each ACT band. The primary ACT selection band for AGNs is 148 GHz. In the 277 GHz plot, the model lines are calculated by scaling the 218 GHz models by a factor that corresponds to the median 218–277 GHz spectral index (-0.33) for all AGNs. On the right, DSFG source counts are shown in each ACT band. The DSFGs are selected from the MMF data. In the 277 GHz plot, the model lines shown in red are calculated by scaling the 218 GHz models by a factor that corresponds to the median 218–277 GHz spectral index (2.7) for MMF sources.

Austermann et al. 2009; Mocanu et al. 2013) is that we use forced photometry in secondary bands. This has the following implication: although our source-recovery simulations, based on primary-band source selection, may indicate that the

secondary bands are reasonably complete in count bins below what would be that band’s detection threshold, our ability to *constrain* the secondary-band flux density of sources that fall in these bins is limited owing to higher noise in the secondary

Table 5
Source Counts

Flux Density ^a (mJy)	AGNs					
	$N/\text{Compl.}_{148}^b$	$N/\text{Compl.}_{218}$	$N/\text{Compl.}_{277}$	$\left(\frac{dN}{dS} S^{5/2}\right)_{148}$	$\left(\frac{dN}{dS} S^{5/2}\right)_{218}$	$\left(\frac{dN}{dS} S^{5/2}\right)_{277}$
8–10	26/0.26	31/0.62	20/0.64	$2.5^{+0.2}_{-0.2}$	$1.3^{+0.2}_{-0.2}$	
10–12	46/0.54	28/0.84	19/0.72	$3.7^{+0.3}_{-0.3}$	$1.5^{+0.3}_{-0.2}$	
12–15	46/0.71	38/0.92	27/0.83	$2.6^{+0.3}_{-0.3}$	$1.9^{+0.3}_{-0.3}$	
15–20	46/0.90	43/0.97	36/0.98	$2.6^{+0.4}_{-0.4}$	$2.2^{+0.3}_{-0.4}$	$1.9^{+0.3}_{-0.3}$
20–30	53/0.98	49/1.00	42/0.99	$3.2^{+0.4}_{-0.4}$	$3.0^{+0.4}_{-0.4}$	$2.5^{+0.4}_{-0.4}$
30–50	56/1.00	49/1.00	40/1.00	$4.9^{+0.6}_{-0.7}$	$4.4^{+0.5}_{-0.6}$	$3.7^{+0.5}_{-0.6}$
50–90	37/1.00	26/1.00	29/1.00	$6.0^{+1.0}_{-1.0}$	$4.0^{+0.8}_{-0.8}$	$4.5^{+0.8}_{-0.9}$
90–170 ^c	34/1.00	15/1.00	13/1.00	7.2 ± 1.2	6.2 ± 1.6	6.6 ± 1.8
170–330	21/1.00	14/1.00	11/1.00	12.2 ± 2.7	12.7 ± 3.4	9.6 ± 2.9
330–650	10/1.00			9.1 ± 2.9		
650–2870	7/1.00	4/1.00	3/1.00	19.6 ± 7.4	13.5 ± 6.7	12.4 ± 7.2
Flux density	DSFGs					
8–10 ^d	2/<0.01	32/0.22	5/<0.01	$0.1^{+0.2}_{-0.2}$	$6.5^{+1.0}_{-1.2}$	
10–12	2/<0.01	28/0.46	8/0.02	$0.2^{+0.1}_{-0.1}$	$4.8^{+1.0}_{-1.0}$	
12–15		31/0.61	20/0.06		$4.1^{+0.8}_{-0.7}$	
15–20	2/0.86	25/0.84	47/0.17	$0.2^{+0.1}_{-0.1}$	$2.6^{+0.6}_{-0.5}$	$31.4^{+4.1}_{-4.1}$
20–25		10/0.91	48/0.38		$1.9^{+0.6}_{-0.6}$	$25.8^{+3.3}_{-3.3}$
25–30		4/0.91	31/0.52		$1.5^{+1.0}_{-0.3}$	$16.5^{+3.3}_{-2.2}$
30–50		4/0.90	31/0.91		$0.7^{+0.5}_{-0.2}$	$5.2^{+0.9}_{-0.9}$
50–90		3/0.90	2/1.00		$1.1^{+0.9}_{-0.3}$	$0.4^{+0.2}_{-0.2}$
90–170			1/1.00			$1.7^{+1.8}_{-0.9}$

Notes.

^a Source counts presented here are calculated by sampling the posterior distributions of the debiased flux densities for all but the bright ($S > 90$ mJy) AGNs (as described in Section 5.2).

^b For each flux density bin, N corresponds to a completeness-corrected median number of sources for that flux density bin. The Compl. value corresponds to the median completeness for the sources in that bin. To calculate the number of sources that would typically be measured in a bin, multiply N by Compl.

^c Above 90 mJy, the 148 GHz AGN counts are reported using the full 950 deg² survey area and measured (not debiased) flux densities. For 218 and 277 GHz, and for 148 GHz below 90 mJy, the counts are reported from a survey area of 505 deg².

^d DSFG counts are reported from the MMF survey area, which covers 277 deg².

band. This effect is most pronounced in the 277 GHz band. The 5 mJy noise in this band is poorly matched to the 2–3 mJy width of source count bins at low flux densities. As pointed out in Mocanu et al. (2013, Section 5), for a 277 GHz catalog selected based directly on S/N in the 277 GHz data, the fraction of sources that falls out of the lowest count bins corrects the counts in those bins for the fraction of the sources that scattered up into the bin from lower flux densities. However, our 277 GHz catalogs are not selected with 277 GHz data, but with the lower-noise 148 GHz data for AGNs and with the MMF for DSFGs. Because the completeness and impurity are not established by 277 GHz selection, the broad 277 GHz flux density posterior distributions that spill out of the lowest count bins overcompensate for sources that may have scattered up into our bins from lower flux densities. We have run simulations that show that this affects our bootstrapped 277 GHz counts that lie 1σ – 2σ from the formal completeness limit (6 mJy for AGNs and 10 mJy for DSFGs) at 277 GHz. In this regime, the counts are biased low. The simulations show that this impacts the three lowest 277 GHz count bins for AGNs and DSFGs, all of which we exclude from the results. This effect may also impact the lowest count bin for AGNs at 218 GHz, which we include, but we caution against over-interpretation of any apparent downward trend in the low end of these counts. We note that in future work the simulations

could be used to quantify the bias and correct the counts, but in this work we conservatively remove the affected flux density bins.

We have addressed the sample purity in three ways. First, in Section 4.4, we considered false detections in maps multiplied by -1 . We concluded that accounting for the few spurious detections in the inverted maps does not impact source counts in a statistically meaningful way. Second, some sources that have intrinsically fainter flux densities could enter into the sample by being boosted above the detection threshold by noise. This is addressed by our use of the full posterior distributions of the debiased flux densities, as discussed above. Third, contamination from Galactic dust could add spurious sources to the catalog that may not be captured by finding sources in an inverted map. We discuss in Section 4.2 the criteria we use to remove sources from the catalog that are likely to be Galactic dust emission. To test for the possibility that residual Galactic dust can mimic sources in our catalogs, we also perform the following analysis. We select regions of the map where we have removed sources that are likely to be Galactic (“Galactic dust-removed regions”). We calculate the source counts from these regions and compare them with the source counts from regions of the map where we find no Galactic sources (“Galactic dust-free regions”). For this test, all sources lie within a decl. range of $\pm 1.2^\circ$ about the celestial

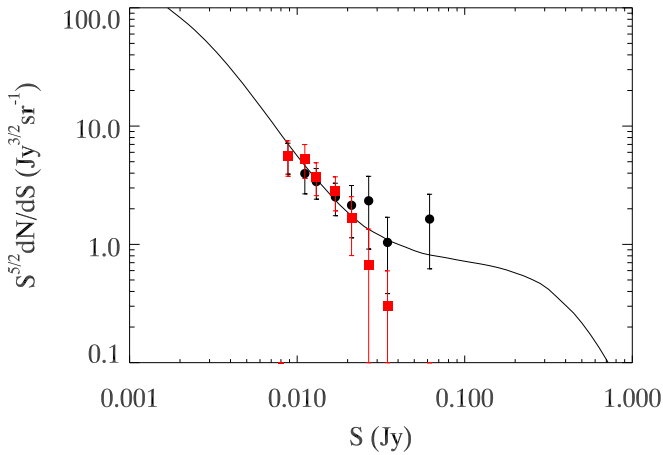


Figure 14. Comparison of “Galactic dust cleaned” and “Galactic dust-free” 218 GHz source counts of dusty galaxies. The red squares represent the counts of ACT sources located in regions of the map from which we have removed Galactic emission using the criteria described in Section 4.2. The black circles represent the counts of ACT sources in regions of the map that appear to be free of Galactic emission, and thus no sources have been removed from these regions. Statistical agreement between the two samples indicates that Galactic contamination does not significantly impact the source counts.

equator. The Galactic dust-removed regions lie in the ranges $03^{\text{h}}20^{\text{m}} < \text{R.A.} < 03^{\text{h}}51^{\text{m}}$, $0^{\text{h}}4^{\text{m}} < \text{R.A.} < 0^{\text{h}}40^{\text{m}}$, $21^{\text{h}}40^{\text{m}} < \text{R.A.} < 22^{\text{h}}40^{\text{m}}$, and $20^{\text{h}}9^{\text{m}} < \text{R.A.} < 21^{\text{h}}$. The Galactic dust-free regions are within ranges of $02^{\text{h}}48^{\text{m}} < \text{R.A.} < 03^{\text{h}}20^{\text{m}}$, $0^{\text{h}}40^{\text{m}} < \text{R.A.} < 01^{\text{h}}44^{\text{m}}$, $23^{\text{h}} < \text{R.A.} < 0^{\text{h}}4^{\text{m}}$, and $21^{\text{h}} < \text{R.A.} < 21^{\text{h}}40^{\text{m}}$. Figure 14 shows the source counts from these dust-free and dust-removed regions. Below 25 mJy, the dust-removed regions tend to have higher source counts than the dust-free regions, but still lie within the 1σ uncertainties. This implies that Galactic dust does not significantly contaminate the source counts of the dusty galaxies. Above 25 mJy, there is marginal tension (2σ) in the distribution of 13 sources between the two regions, favoring more sources in the dust-free regions. Therefore, this is still consistent with no contamination from Galactic emission. Interpretation of this as evidence for incompleteness due to Galactic cuts is disfavored by simulations (Figure 6, red curves).

5.2.2. Discussion of Source Counts

The models that describe the synchrotron source counts are based on statistical extrapolations from lower-frequency radio source counts (i.e., 5 GHz). Tucci et al. (2011) provide models using different physically motivated prescriptions for the spectral behavior of the sources. They include three populations of sources, as classified by their 1–5 GHz spectral indices: steep spectrum ($\alpha < 1$), inverted spectrum ($\alpha > 1$), and flat spectrum ($\alpha \sim 0$). The latter include subpopulations of both BL Lacs and FSRQs. The models differ in the frequency at which there is a break in the synchrotron spectrum for the flat-spectrum sources. The break frequency indicates the transition from optically thick to optically thin synchrotron emission and thus is related to the size of the region at which this transition occurs. For the Tucci et al. (2011) C1 model, BL Lacs and FSRQs both have the same size transition region, between 0.01 and 10 pc. For their C2Co model, the transition region is more compact in FSRQs than in BL Lacs. For their C2Ex model, the region is more extended in FSRQs than in BL Lacs. Although they do not provide 277 GHz models, we have

scaled their 218 GHz models up to 277 GHz using the median spectral index for the sample.

We find that the preferred Tucci et al. (2011) model, the C2Ex model, underpredicts the 148 GHz synchrotron source counts, most noticeably in the intermediate flux density range of ~ 10 to ~ 100 mJy (see Figure 13). Our results in this range agree with the number counts in Mocanu et al. (2013), who noted this discrepancy with the C2Ex model. When we calculate how many sources the model would predict given our survey area and completeness and compare with the counts in each flux density bin, the χ^2 of the fit of the C2Ex model to our 148 GHz data is 51.3, with 11 degrees of freedom. Other models presented by Tucci et al. (2011) perform better. The fits of the C1 model and the C2Co model produce χ^2 of 21.5 and 22.3, respectively. None of the models are formally good fits, but the C1 and C2Co are much better than the C2Ex. The preference for the C2Ex model in Tucci et al. (2011) is driven by the better fit to the >0.5 Jy number counts from Planck Collaboration et al. (2011c) at 148 and 220 GHz. We note that these were based on the early release catalogs, which agree (but with larger uncertainties) with the counts of the intermediate catalogs (Planck Collaboration et al. 2013, shown in Figure 13). These results may indicate differences in the spectral behavior of the AGN populations that contribute to the intermediate versus the brightest number counts.

The models for the dusty sources are from Béthermin et al. (2011, 2012) and Cai et al. (2013). Béthermin et al. (2011) use a parametric backward evolution model to describe the cosmological evolution of the luminosity function of infrared galaxies. Cai et al. (2013) combine a descriptive backward parametric model for late-type galaxies and AGNs below a redshift of 1.0 with a physically motivated forward model for the evolution of spheroids and AGNs above a redshift of 1.5. At the bright end, a population of lensed dusty galaxies is expected to dominate the source counts. Toward fainter flux densities, the unlensed component becomes more important. At 277 GHz, we also show (in red) models from 218 GHz that have been scaled up to 277 GHz by the median 218–277 GHz spectral index for the sample.

We find good agreement between the DSFG source counts and the models for sources with 218 GHz flux densities above ~ 20 mJy (see Figure 13). These brighter sources are expected to be drawn from a strongly lensed source population, and the lensed nature of these sources is being tested and confirmed with follow-up observations (see Appendix A). The ACT source counts also agree well with the >20 mJy counts from SPT (Mocanu et al. 2013).³¹ At lower flux densities (~ 8 – 13 mJy at 218 GHz), the ACT sample is likely starting to probe the bright end of the unlensed source population. The 218 GHz source counts data continue to agree well with the models at the faint end, where the more sensitive ACT data push below the limits of current surveys.

The 277 GHz DSFG source counts presented here are the first published in this flux density range. The source counts at fainter flux densities are constrained by observations from

³¹ In addition to SPT counts of DSFGs, counts at ~ 218 GHz are provided in Planck Collaboration et al. (2013). They lie well above both the model predictions and the ACT and SPT counts and are at higher fluxes. Note, however, that the Planck counts were based on the Early Release Compact Source Catalog, which may have been contaminated by Galactic cirrus. Planck’s later PCCS2 catalog (Planck Collaboration et al. 2016) has improved on the identification and removal of Galactic dust emission, but the collaboration has not published revised source counts.

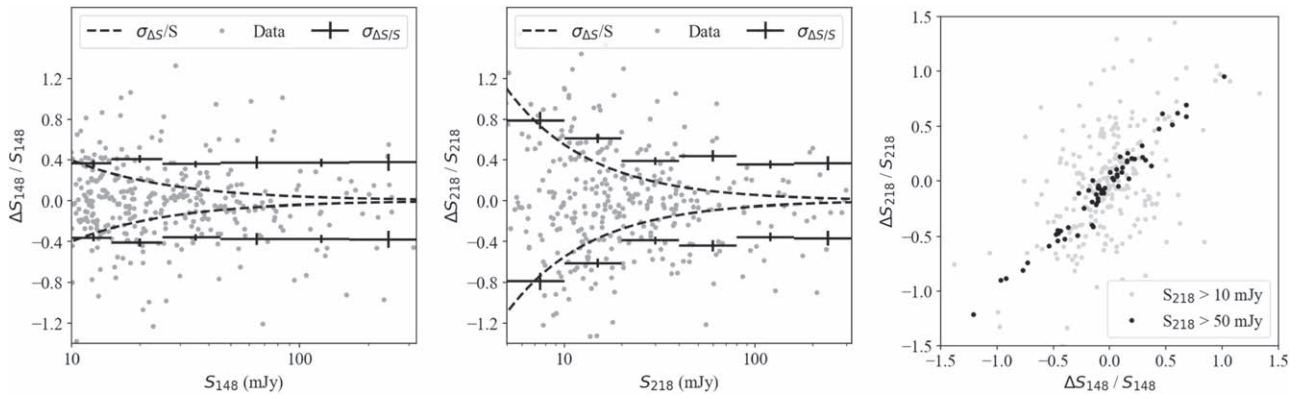


Figure 15. Variability of AGN emission. The left and middle panels show, for 148 and 218 GHz, the fractional deviation in flux density between 2009 and 2010. The dashed curve shows the prediction for the rms deviation due to map noise. The points with error bars show flux-density-binned estimates of the rms deviation of the sample. At low flux densities the interyear variation is consistent with noise, but at higher flux densities the intrinsic source variability dominates at 40%. The right panel shows that the variations in the two bands closely track one another in the flux density regime (>50 mJy), where intrinsic variability dominates.

AzTEC in two regions: COSMOS (Austermann et al. 2009) and SHADES (Austermann et al. 2010). These earlier studies were in some tension with one another, and the dispersion among the models reflects this. Our higher flux density data prefer the higher models, but none lie within perfect agreement in this new regime.

5.3. Variability

The emission from blazars shows significant variability correlated across the electromagnetic spectrum that can give insights into the processes (e.g., turbulence) in the AGN jet (e.g., Burbidge & Hewitt 1992; Hughes et al. 1992; Aller 1999; Tingay et al. 2003; Ciprini et al. 2007; Abdo et al. 2010; Riordan et al. 2017; Fan et al. 2018). To probe AGN variability of this sample, we include in the extragalactic catalog per-year flux density estimates for AGN-classified sources selected at 148 GHz (i.e., $\sim 95\%$ of AGNs). Specifically 148 GHz and 218 GHz raw flux densities (not debiased) are provided separately for the observing seasons 2009 and 2010. Figure 15 summarizes these data. The left and middle panels show the rms (68% c.l.) fractional deviation in flux densities between years (indicated by data points), along with the expected rms deviation due to map noise (indicated by the dashed line). The error on the rms deviation data is computed with a bootstrap Monte Carlo within each bin. At the lowest flux densities (and thus lowest S/N), the observed rms deviation is consistent with the expectation from noise. However, above 30 mJy, the interyear scatter becomes dominated by source variability with an rms deviation at the 40% level. This is true for both the 148 GHz and the 218 GHz frequency bands. The 40% rms deviation shows no dependence on flux density.

We note that miscalibration can produce an overall shift between years; however, the systematic uncertainties at 148 and 218 GHz are at the percent level, negligible compared to the 40% variation observed. Furthermore, a significant systematic would produce an asymmetry around zero flux density in the left and middle panels of Figure 15, an asymmetry that is not observed.

The right panel of Figure 15 shows that the flux density variations are strongly correlated between bands at flux densities (>50 mJy), where the source variability completely dominates. For the fractional flux density variation in these brightest sources, the interband correlation coefficient is 0.98.

6. DSFGs: A Closer Look

A subset of the brightest lensed DSFG candidates was selected from an early version of the ACT equatorial source catalog for multiwavelength follow-up. Specifically, ACT maps at 218 GHz were matched-filtered (Section 3.1), and the brightest 36 sources with dust-like spectra (Section 5.1) and without clear contamination from Galactic dust were selected. The size of the original sample was chosen to be large enough to enable statistical inferences about source properties, but not so large as to render impractical the extensive (and thus formidable) multiwavelength follow-up observations required to understand each source. In this initial selection, we also vetoed any sources cross-identified with nearby star-forming galaxies resolved in optical imaging from SDSS. Later, the introduction of systematic cuts for Galactic contamination (Section 4.2) and the availability of the 277 GHz data were used to discard six candidates that were unlikely true extragalactic sources. The resulting sample of the brightest 30 lensed DSFG candidates are all significant ($S/N > 6$) unresolved detections with 218 GHz flux greater than 16 mJy and a dust-like spectrum spanning all three ACT frequency bands. Partial catalog entries for these DSFGs are given in Table 6. The three-band selection indicates with high confidence that these are all real DSFGs. Indeed, two are well-studied, lensed DSFGs. The first is ACT-S J2135–0102, the so-called “Cosmic Eyelash,” with lensing magnification $\mu = 32$ at $z = 2.359$ (Swinbank et al. 2010). Interestingly, we also see evidence for the 150 GHz SZ decrement of the massive lens associated with the Eyelash (Table 6). The second is ACT-S J020941+001557 with $\mu \approx 10$ at $z = 2.553$ (Geach et al. 2015; Su et al. 2017; Geach et al. 2018; Rivera et al. 2019). A third, ACT-S J202955+012054, we have also confirmed as a lensed system at $z = 2.64$ with a CO spectral line energy distribution characteristic of a ULIRG/AGN with a potential galaxy-scale outflow (Roberts-Borsani et al. 2017). In the remainder of this section and in Appendix A, we discuss additional data characterizing this brightest sample of DSFGs.

In Su et al. (2017), we took a preliminary step toward characterizing the redshift distribution and physical properties of ACT-selected DSFG candidates. We modeled ACT and *Herschel*-SPIRE photometry to derive characteristics for 9 of our 30 sources that fell in the footprint of either the *Herschel* Stripe 82 Survey (HerS; Viero et al. 2014) or the HerMES Large Mode Survey (HeLMS; Oliver et al. 2012). We

Table 6
Partial Catalog Entries for ACT DSFGs Selected for Detailed Study

ACT-S ID ^a (J2000)	S/N	α_{148}^{218b}	α_{218}^{277}	S_{148} (mJy)	S_{218} (mJy)	S_{277} (mJy)
001133–001835	6.6	3.4 (3.3 ^{+1.2} _{-0.9})	0.7 (1.1 ^{+1.2} _{-1.3})	5.9 ± 2.2 (5.3 ^{+2.1} _{-1.9})	22.1 ± 3.4 (20.0 ^{+3.2} _{-3.7})	26.3 ± 8.2 (24.4 ^{+6.9} _{-6.4})
002220–015523	6.5	4.3 (4.2 ^{+1.1} _{-0.9})	1.8 (2.2 ^{+0.9} _{-0.8})	5.2 ± 2.2 (5.0 ^{+2.0} _{-1.8})	27.2 ± 4.2 (26.3 ^{+3.3} _{-4.2})	41.5 ± 5.4 (41.9 ^{+5.2} _{-5.1})
003814–002255	10.7	3.0 (3.0 ^{+0.8} _{-0.7})	1.9 (2.0 ^{+0.8} _{-0.8})	7.6 ± 1.8 (7.1 ^{+1.8} _{-1.7})	24.6 ± 2.7 (23.5 ^{+2.7} _{-3.8})	39.1 ± 5.5 (36.9 ^{+5.3} _{-5.3})
003929+002422	8.9	3.2 (3.1 ^{+1.1} _{-1.0})	2.1 (2.2 ^{+1.1} _{-1.0})	5.7 ± 1.8 (5.1 ^{+1.8} _{-1.6})	20.0 ± 2.7 (17.7 ^{+3.9} _{-4.5})	33.4 ± 5.5 (29.9 ^{+5.3} _{-5.2})
004410+011818	13.3	2.8 (2.8 ^{+0.5} _{-0.5})	2.9 (3.1 ^{+0.6} _{-0.5})	12.1 ± 1.7 (11.7 ^{+1.8} _{-1.7})	35.7 ± 2.7 (34.7 ^{+3.6} _{-4.7})	71.0 ± 5.1 (70.9 ^{+5.0} _{-5.0})
004532–000127	11.1	3.8 (3.8 ^{+0.9} _{-0.8})	2.1 (2.1 ^{+0.9} _{-0.8})	5.9 ± 1.8 (5.6 ^{+1.7} _{-1.7})	25.9 ± 2.8 (25.0 ^{+3.5} _{-4.3})	42.4 ± 5.6 (40.7 ^{+5.4} _{-5.3})
010729+000114	7.3	6.2 (4.7 ^{+1.5} _{-1.3})	1.6 (1.8 ^{+1.3} _{-1.0})	1.6 ± 1.8 (2.2 ^{+1.4} _{-1.0})	18.5 ± 2.8 (15.8 ^{+3.6} _{-4.2})	27.1 ± 5.5 (23.0 ^{+5.0} _{-5.0})
011640–000457	10.8	2.8 (2.8 ^{+0.8} _{-0.8})	2.5 (2.6 ^{+0.9} _{-0.9})	7.7 ± 1.8 (7.2 ^{+1.7} _{-1.7})	22.8 ± 2.7 (21.2 ^{+3.8} _{-4.3})	42.0 ± 5.4 (39.9 ^{+5.3} _{-5.3})
013857+021420	8.9	2.8 (2.9 ^{+0.6} _{-0.5})	...	14.2 ± 2.9 (13.5 ^{+2.9} _{-2.8})	41.9 ± 4.7 (41.1 ^{+3.2} _{-3.6})	...
020941+001557	35.5	3.7 (3.7 ^{+0.3} _{-0.3})	3.1 (3.6 ^{+0.2} _{-0.2})	17.2 ± 1.8 (17.0 ^{+1.8} _{-1.7})	71.5 ± 2.7 (71.1 ^{+2.6} _{-2.6})	152.0 ± 5.4 (169.1 ^{+5.3} _{-5.3})
022830–005226	14.1	3.1 (3.0 ^{+0.7} _{-0.6})	3.0 (3.4 ^{+0.5} _{-0.5})	8.5 ± 1.8 (8.1 ^{+1.7} _{-1.7})	28.7 ± 2.9 (26.7 ^{+3.0} _{-3.0})	58.8 ± 5.3 (59.5 ^{+5.2} _{-5.2})
023120+011636	6.5	3.3 (3.0 ^{+1.2} _{-1.2})	1.6 (2.9 ^{+1.2} _{-1.2})	5.1 ± 1.7 (4.4 ^{+1.7} _{-1.6})	18.1 ± 2.8 (14.2 ^{+2.8} _{-3.8})	26.8 ± 4.6 (26.6 ^{+4.5} _{-4.5})
025331–000318	27.7	3.4 (3.4 ^{+0.3} _{-0.3})	2.8 (3.2 ^{+0.3} _{-0.3})	15.9 ± 1.8 (15.7 ^{+1.8} _{-1.8})	59.0 ± 2.9 (58.1 ^{+3.0} _{-3.8})	114.8 ± 5.4 (125.5 ^{+5.3} _{-5.3})
025512–011456	7.2	3.0 (2.9 ^{+1.0} _{-1.0})	2.2 (2.9 ^{+1.7} _{-1.6})	6.1 ± 1.7 (5.5 ^{+1.7} _{-1.6})	19.4 ± 2.7 (16.8 ^{+4.2} _{-6.4})	32.7 ± 5.0 (32.6 ^{+4.8} _{-4.8})
030410+013225	6.6	5.0 (4.0 ^{+1.5} _{-1.5})	4.1 (4.6 ^{+1.5} _{-1.1})	2.5 ± 1.7 (2.3 ^{+1.5} _{-1.1})	17.6 ± 2.6 (13.4 ^{+4.5} _{-6.8})	46.7 ± 7.6 (44.6 ^{+7.4} _{-7.4})
031019–000215	8.6	8.3 (5.5 ^{+1.4} _{-1.2})	1.9 (1.9 ^{+0.9} _{-0.9})	0.8 ± 1.8 (2.1 ^{+1.2} _{-0.9})	21.1 ± 2.9 (19.4 ^{+3.7} _{-3.7})	33.1 ± 5.1 (29.9 ^{+4.9} _{-4.8})
031127+013639	12.8	4.1 (4.1 ^{+0.8} _{-0.7})	2.9 (3.1 ^{+0.7} _{-0.7})	7.0 ± 1.9 (6.8 ^{+1.8} _{-1.8})	34.4 ± 2.7 (33.5 ^{+3.6} _{-3.2})	69.5 ± 10.4 (69.3 ^{+10.0} _{-9.8})
032104+012934	6.2	5.7 (4.2 ^{+1.6} _{-1.5})	0.7 (2.9 ^{+1.7} _{-1.7})	1.8 ± 1.7 (2.0 ^{+1.7} _{-1.7})	16.6 ± 2.7 (12.2 ^{+4.6} _{-5.0})	19.6 ± 6.1 (19.8 ^{+5.6} _{-5.7})
032121–000221	11.9	2.8 (2.8 ^{+0.8} _{-0.7})	3.1 (3.2 ^{+0.8} _{-0.8})	7.9 ± 1.8 (7.4 ^{+1.8} _{-1.7})	23.7 ± 2.9 (22.3 ^{+4.4} _{-4.1})	49.6 ± 5.2 (48.7 ^{+5.0} _{-5.1})
032351+012801	8.9	4.1 (4.0 ^{+1.0} _{-0.9})	0.7 (1.7 ^{+1.2} _{-1.1})	4.8 ± 1.6 (4.6 ^{+1.5} _{-1.5})	23.8 ± 2.7 (22.1 ^{+4.0} _{-4.4})	27.9 ± 5.8 (29.3 ^{+5.3} _{-5.3})
034003+001627	8.0	4.1 (3.7 ^{+1.3} _{-1.2})	2.3 (2.4 ^{+1.2} _{-1.1})	3.7 ± 1.8 (3.4 ^{+1.6} _{-1.4})	18.1 ± 2.8 (15.3 ^{+3.8} _{-4.5})	31.1 ± 5.1 (27.1 ^{+4.9} _{-4.8})
034228–005644	8.9	2.5 (2.3 ^{+1.0} _{-1.0})	3.0 (3.2 ^{+1.2} _{-1.0})	6.8 ± 1.8 (6.0 ^{+1.8} _{-1.7})	17.7 ± 2.8 (14.5 ^{+4.1} _{-4.9})	36.6 ± 5.2 (33.0 ^{+5.1} _{-5.0})
202955+012054	7.4	2.9 (2.8 ^{+1.0} _{-0.8})	3.3 (3.7 ^{+0.9} _{-0.9})	7.2 ± 2.0 (6.6 ^{+2.0} _{-2.0})	22.0 ± 3.0 (19.8 ^{+3.2} _{-4.1})	48.6 ± 5.8 (48.0 ^{+5.6} _{-5.6})
212740+010921	8.7	5.2 (4.6 ^{+1.4} _{-1.1})	1.7 (1.8 ^{+1.0} _{-1.0})	3.0 ± 2.1 (3.3 ^{+1.7} _{-1.4})	22.8 ± 2.9 (21.1 ^{+3.9} _{-3.9})	34.2 ± 6.0 (31.3 ^{+5.7} _{-5.6})
213511–010255	14.9	... (7.5 ^{+1.2} _{-1.1})	3.8 (4.0 ^{+0.5} _{-0.5})	-3.2 ± 2.1 (1.8 ^{+1.9} _{-1.9})	34.8 ± 3.0 (34.1 ^{+3.7} _{-3.6})	85.4 ± 6.8 (90.3 ^{+6.7} _{-6.7})
213713+011156	8.2	2.8 (2.8 ^{+1.0} _{-0.8})	1.4 (1.5 ^{+1.1} _{-1.1})	7.1 ± 2.1 (6.4 ^{+2.0} _{-2.0})	21.1 ± 3.0 (19.5 ^{+3.3} _{-3.8})	29.9 ± 5.7 (26.6 ^{+5.3} _{-5.1})
230239–013333	6.8	3.7 (3.6 ^{+1.2} _{-1.0})	3.2 (3.5 ^{+0.9} _{-0.7})	6.1 ± 2.5 (5.6 ^{+2.3} _{-2.1})	25.1 ± 3.7 (23.6 ^{+3.2} _{-4.2})	53.8 ± 6.6 (53.3 ^{+6.3} _{-6.4})
231252–001524	7.3	... (6.2 ^{+1.4} _{-1.3})	1.7 (1.8 ^{+1.0} _{-1.0})	-2.2 ± 2.1 (1.6 ^{+1.0} _{-0.7})	21.3 ± 3.1 (19.6 ^{+3.3} _{-3.7})	31.9 ± 6.1 (28.7 ^{+5.7} _{-5.5})
231356+010910	7.7	4.5 (4.0 ^{+1.4} _{-1.2})	1.9 (2.0 ^{+1.2} _{-1.1})	3.3 ± 2.0 (3.2 ^{+1.7} _{-1.4})	19.4 ± 2.9 (16.8 ^{+3.8} _{-4.4})	30.6 ± 5.7 (26.8 ^{+5.3} _{-5.3})
231643–011325	6.4	8.6 (4.6 ^{+1.7} _{-1.7})	2.6 (3.5 ^{+1.4} _{-1.1})	0.6 ± 1.9 (1.6 ^{+1.3} _{-0.9})	18.2 ± 2.9 (14.2 ^{+4.2} _{-7.0})	34.0 ± 6.1 (33.2 ^{+5.9} _{-5.8})

Notes.

^a The ACT-S ID encodes the sexagesimal position of each source (hhmmss ± ddmms).

^b For interband spectral indices ($\alpha_{\lambda}^{\lambda}$) and flux densities (S_{λ}), raw (debiased) values are given outside (inside) parentheses.

emphasize that while these sources were detected by *Herschel* (Asboth et al. 2016; Nayyeri et al. 2016), only ACT data were used in the subsample selection. When fitting the far-infrared SED of the thermal emission for warm extragalactic dust, one has a range of models from which to choose, each with different physical implications. In Su et al. (2017) we explored four different models with different assumptions about dust temperature distribution and opacity. Independent of model choice, we found that the subsample has a redshift range $z = 2.5\text{--}5.5$ covering the era leading up to “cosmic noon,” when the star formation density of the universe peaked (e.g., Burgarella et al. 2013). High apparent infrared luminosities $\mu L_{\text{IR}} = (0.3\text{--}1.4) \times 10^{14} L_{\odot}$ (as above, μ here is lensing magnification) imply apparent star formation rates significantly greater than $1000 M_{\odot} \text{ yr}^{-1}$ (neglecting possible AGN contribution). These luminosities are consistent with other samples that have apparent brightness enhanced by strong lensing with $\mu \sim 10$ (e.g., Bussmann et al. 2013; Weiß et al. 2013; Cañameras et al. 2015; Harrington et al. 2016; Strandet et al. 2016). Finally, our modeling showed that the common assumption of optically thin dust is not a good match at the

peak of the SED (rest-frame wavelength $\sim 100 \mu\text{m}$) for ACT-selected sources.

Beyond SED modeling, we have been compiling a suite of multifrequency data from both our own follow-up observations and archival data sets. In Appendix A we present optical and infrared imaging for the 30 brightest DSFG candidates along with locations of radio, millimeter, and submillimeter counterparts. Based on these results, compelling evidence already exists that a number of sources, identified at higher resolution with a combination of radio, millimeter, and submillimeter data, are lensed by galaxies or galaxy clusters detected in the optical and/or infrared data. A number of these systems with well-measured redshifts are undergoing detailed spectral line imaging and will be the subject of future publications.

7. Conclusions

We have presented an extragalactic source catalog of AGNs and DSFGs from the ACT 2009–2010 survey of the celestial equator. The multifrequency (148, 218, and 277 GHz) data set is unique in its combination of survey area covering hundreds of square degrees and sensitivity to DSFGs. For AGNs, the 277 GHz

data provide new constraints. Therefore, the catalog extends previous galaxy population studies by ACT (Marriage et al. 2011; Marsden et al. 2014; Datta et al. 2019), SPT (Vieira et al. 2010; Mocanu et al. 2013), and Planck (Cañameras et al. 2015; Planck Collaboration et al. 2016). It complements deeper, degree-scale millimeter surveys (e.g., Austermann et al. 2009, 2010; Staguhn et al. 2014) and submillimeter surveys (e.g., Negrello et al. 2010; Bussmann et al. 2013; Wardlow et al. 2013; Asboth et al. 2016; Nayyeri et al. 2016; Netke et al. 2017). In addition to the galaxy catalogs, all maps, including the equatorial 277 GHz data set for the first time, are publicly available.

The heterogeneous selection in the presence of Galactic emission presents challenges to maintain sample purity and handle Eddington bias, especially for DSFGs with the lowest flux densities. We have overcome these challenges by developing custom tests for Galactic contamination and a method for debiasing flux densities that accounts for arbitrary selection effects.

Based on the resulting extragalactic catalog, we presented spectral properties and source counts for the AGNs and DSFGs. For AGNs, we have shown that the previously measured spectral slope between 148 and 218 GHz extends to 277 GHz. For DSFGs, we have shown that the average spectrum departs from a single-temperature, optically thin graybody above 218 GHz. This may be due to the emission becoming optically thick or indicate an additional cold dust component. In terms of source counts, we present the first blazar source counts at 277 GHz and find consistency with count models extrapolated from models built for data at lower frequencies. For DSFGs, we extend the existing 218 GHz counts to lower flux density, where unlensed sources dominate; we find good agreement with source models here. At 277 GHz the DSFG counts extend to higher flux densities than previously published and are higher than most models predicted for 277 GHz.

We have estimated the interyear fractional deviation in flux density of the blazar population and found it to be 40% for sources with flux densities above 50 mJy in both the 148 and 218 GHz bands. Furthermore, we find this variability to be tightly correlated between the bands, with a correlation coefficient of 0.98.

Thirty of the brightest DSFGs are described in detail. These have been the subject of more detailed study (Roberts-Borsani et al. 2017; Su et al. 2017; Rivera et al. 2019). Appendix A describes radio to optical data on these sources. Interestingly, an apparent SZ decrement at 148 GHz is coincident with two of the sources (likely associated with massive lenses).

Looking ahead, the ACTPol receiver has been upgraded as Advanced ACT with additional bands that will span 30–250 GHz. The resulting survey, covering thousands of square degrees to sensitivities surpassing the current work, will contribute to the next generation of wide-field millimeter-wave extragalactic catalogs.

This work was supported by the U.S. National Science Foundation through awards AST-0408698 and AST-0965625 for the ACT project, as well as awards PHY-0855887 and PHY-1214379. Funding was also provided by Princeton University, the University of Pennsylvania, and a Canada Foundation for Innovation (CFI) award to UBC. ACT operates in the Parque Astronómico Atacama in northern Chile under the auspices of the Comisión Nacional de Investigación Científica y Tecnológica de Chile (CONICYT). Computations were performed on the GPC

supercomputer at the SciNet HPC Consortium. SciNet is funded by the CFI under the auspices of Compute Canada, the Government of Ontario, the Ontario Research Fund—Research Excellence, and the University of Toronto. In our use of observations from the SMA, the authors are grateful to the people of Hawai‘ian ancestry on whose sacred mountain we are privileged to be guests. Some of the observations reported in this work were obtained with the Southern African Large Telescope (SALT). Funding for SALT is provided in part by Rutgers University, a founding member of the SALT consortium. M.G. and T.M. acknowledge support from Johns Hopkins University. A.J.B. and J.R. acknowledge support from NSF grant AST-0955810. K.M. acknowledges support from the National Research Foundation of South Africa (grant No. 93565). D.C. acknowledges the financial assistance of the South African SKA Project (SKA SA) toward this research (www.ska.ac.za). R.D., P. A., F.R., and G.M. received funding from the Chilean grants FONDECYT 11100147 and BASAL (CATA). R.D. acknowledges CONICYT for grants FONDECYT 1141113, Anillo ACT-1417, QUIMAL 160009, and BASAL PFB- 06 CATA. C.L. thanks CONICYT for grant Anillo ACT-1417. This research made use of Astropy, a community-developed core Python package for Astronomy (Astropy Collaboration et al. 2013), and the Astronomy IDL Library (Landsman 1993).

Appendix A Auxiliary Data for Brightest DSFGs

This appendix provides a closer look at the 30 sources selected as candidate lensed DSFGs for a campaign of multifrequency follow-up (Section 6).³² For each source we show optical and infrared imaging that, in many cases, reveals a putative lens galaxy and, in fewer cases, shows evidence for the light from a lensed DSFG. The optical images are from the Panoramic Survey Telescope and Rapid Response System (Pan-STARRS) 1 data release, in the r ($\lambda = 622$ nm; $m = 23.2$ 5σ depth; $1''.19$ seeing), i ($\lambda = 763$ nm; $m = 23.1$ 5σ depth; $1''.11$ seeing), and z ($\lambda = 905$ nm; $m = 22.3$ 5σ depth; $1''.07$ seeing) bands (Chambers et al. 2016). We have chosen to show Pan-STARRS imaging instead of the deeper stacked imaging from the SDSS Stripe 82 because the better seeing in Pan-STARRS enables clearer distinction of lensing features. The near-infrared K_s -band ($\lambda \approx 2.1$ μm) images are either from the VISTA Hemispheres Survey (McMahon et al. 2013) with a 5σ detection limit of $m = 18.1$ (Vega) or from our own follow-up observations with the NICFP camera (Vincent et al. 2003) on the ARC 3.5 m telescope at the Apache Point Observatory (APO) with a K_s -band 5σ detection limit of $m = 19.5$ (Vega). At longer wavelengths, imaging is provided either by the *Wide-field Infrared Survey Explorer* all-sky survey in bands W1 ($\lambda \approx 3.5$ μm) and W2 ($\lambda \approx 4.5$ μm) (Wright et al. 2010) or, where available, by the *Spitzer* Heritage Archive,³³ for which the analogous bands (same wavelengths) are called S1 and S2. Most *Spitzer* data derive from the *Spitzer* IRAC Equatorial Survey (Timlin et al. 2016) and the *Spitzer*-HETDEX Exploratory Large-Area Survey (S1, S2) (Papovich et al. 2016).

The images are annotated to indicate the locations of detections from the radio to the submillimeter, according to the

³² The full set of 30 sources is available in the online version (doi:10.3847/1538-4357/ab7915).

³³ <http://sha.ipac.caltech.edu/applications/Spitzer/SHA/>



Figure 16. DSGF symbol legend. Symbols indicate the location of detections in the centimeter (VLA), millimeter (ACT, SMA), and submillimeter (SPIRE) bands. Sizes of symbols indicate positional uncertainty (1σ) associated with the detection. Sources may lack detections by VLA, SMA, and/or SPIRE.

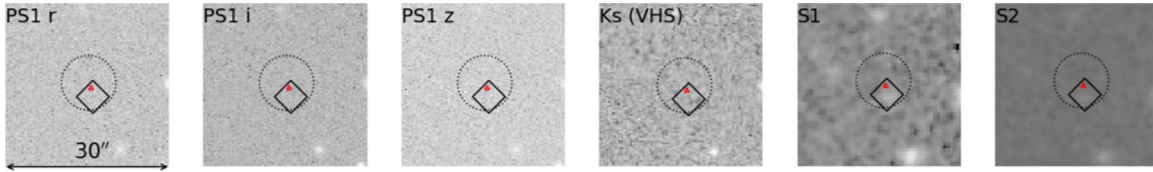


Figure 17. ACT-S J001133–001835 has no associated radio emission (only FIRST data available). Furthermore, the optical and infrared imaging shows no evidence for a lens near the SMA location. A fit to the ACT and *Herschel* photometry gives a DSGF redshift $z \approx 3.3$, temperature $T \approx 46$ K, and apparent luminosity $\mu L_{\text{IR}} \approx 10^{13.7} L_{\odot}$ (Su et al. 2017, where the source is listed as ACT-S J0011–0018). The full set of 30 components is available in the Figure Set.

(The complete figure set (30 images) is available.)

symbol legend shown in Figure 16. The sizes of the annotations indicate the astrometric errors associated with the corresponding detections ($5''$ for ACT, $3''$ for *Herschel*, $1''$ for radio data, and $<0''.5$ for SMA Su et al. 2017). Where the sample overlaps the *Herschel* Stripe 82 Survey (HerS; Viero et al. 2014) and the HerMES Large Mode Survey (HeLMS; Oliver et al. 2012), there are *Herschel* detections (solid black diamonds) for nine sources at $\lambda = 250, 350,$ and $500 \mu\text{m}$ (Su et al. 2017). Millimeter-wave detections are provided by ACT (dashed circle; $\lambda = 2, 1.4,$ and 1.1 mm) and by our follow-up observations with the Submillimeter Array (SMA; red rectangle; $\lambda = 1.4$ mm). The subarcsecond astrometry of the SMA imaging makes it the most reliable indicator of the DSGF position. Details of the SMA imaging will be given in a future publication. Finally, nearby radio detections (blue pentagons) are selected from (in order, as available) (1) our own deep follow-up with the Jansky VLA (JVLA) at ($\lambda = 6$ cm; rms $25 \mu\text{Jy beam}^{-1}$; VLA/13A-478, PI M. Gralla); (2) the VLA SDSS Stripe 82 Survey at 1.4 GHz (herein referred to as VLASS821P4; $\lambda = 21$ cm; rms $52 \mu\text{Jy beam}^{-1}$; Hodge et al. 2011); or (3) the VLA Faint Images of the Radio Sky at Twenty Centimeters (FIRST; rms $150 \mu\text{Jy beam}^{-1}$) survey (Becker et al. 1995; White et al. 1997).

Accompanying the annotated images in Figure 17, we also provide a written synopsis of what is known about each source and its lens candidate. As the data permit, these synopses clarify radio associations, give details of SED modeling, provide redshift estimates for the source and/or lens, and point out unique source properties. To establish redshifts for a subset of putative lens galaxies, we use SDSS (Alam et al. 2015) and our own spectroscopy with the South African Large Telescope (SALT; Buckley et al. 2006) (PI J. Hughes; for details of the observational setup, data reduction, and analysis of the SALT/RSS spectra, see Roberts-Borsani et al. 2017). These images and synopses provide an initial look at the sources of this sample, and further studies (e.g., CO mapping) are underway.

Appendix B

Millimeter Spectral Indices: Special Cases

The sources discussed in this appendix have unusual millimeter spectral indices given their ACT measurements. We investigated these sources using optical data from SDSS and archival data from NED, and we visually inspected them in

the ACT maps. Beyond curiosity, there were two main motivations for these investigations. First, sources with 148–218 GHz spectral indices that lie in between the AGN and DSGF populations could be misidentified, so the extra information could potentially clarify source categorization. Second, the debiasing methods we adopt when determining flux densities for the secondary bands assume that sources are drawn from either AGN or DSGF populations that have spectral index distributions approximated by Gaussians. For sources that have very atypical spectra, these assumptions are unlikely to hold, and thus their raw secondary-band flux densities would be more reliable than what is reported as debiased. On a population level, if there are a substantial number of outliers that are misidentified or otherwise skewing the properties of the measured spectral index distributions for either the AGNs or the DSGFs, this would make our debiasing less optimal.

We first restrict attention to the area of the map that has reliable and comparatively low-noise measurements in all three ACT bands, which is within $-1.2^\circ < \text{decl.} < 1.2^\circ$. We then identify four groups of special cases: sources that have $0.5 < \alpha_{148-218} < 1.5$, AGNs with $\alpha_{218-277} < -5$, DSGFs with $\alpha_{218-277} > 5$, and DSGFs with $\alpha_{218-277} < 0$.

Sources that have $0.5 < \alpha_{148-218} < 1.5$ are near the boundary between AGNs and DSGFs, which we draw at $\alpha_{148-218} = 1.0$. In this clean area of the maps, there are 13 such sources. All appear to be well measured in the ACT data. An inspection of optical images from SDSS reveals that two coincide with large nearby elliptical galaxies, one at $z = 0.07$ with a known 4C radio source, and the other at $z = 0.017$. These have $\alpha_{148-218} < 1.0$ and so are (correctly) classified as AGNs. Another, ACT-S J000910–003652, has a pair of galaxies within the ACT beam. The $\alpha_{148-218}$ for this source is 1.2, so it is classified as a DSGF. Both galaxies in this pair are at $z = 0.07$, and one is a spiral galaxy and the other contains a known AGN. We note that the CO $J(2-1)$ line at 230.5 GHz can fall within the ACT 218 GHz band. The ACT 218 GHz band is 17.0 GHz wide, with central frequency at 219.7 GHz (Swetz et al. 2011). If we approximate the band transmission as a step function, the CO line will fall within the ACT band for sources in the range $0.01 < z < 0.09$. Thus, if present, some CO line emission could increase their 218 GHz flux density relative to their 148 GHz flux density and thus move a more typical AGN spectral index toward the dusty galaxy spectral















index. In addition to these nearby galaxies, one of the other source fields contains a QSO at $z = 1.77$, and the corresponding ACT AGN has $\alpha_{148-218} = 0.5$. The remaining nine fields do not contain unambiguous matches.

There are seven AGNs with very steep $\alpha_{218-277} < -5$. All are undetected and basically have no flux density at 277 GHz ($S/N < 1\sigma$), and all but one have 218 GHz $S/N < 5$ as well. All have known radio counterparts in NED, with measurements in the 4C, NVSS, PMN, and/or GBT surveys. One of these is a radio-bright star, V0711 Tau.

There are seven DSFGs with $\alpha_{218-277} > 5$. As might be anticipated given their spectra, these all have 218 GHz $S/N < 3.5$, with more significant $S/N > 5$ detections at 277 GHz. None are in compromised or dusty locations in the ACT maps. Two are nearby spiral galaxies, ACT-S J235106+010318 and ACT-S J214129+005340. The SDSS imaging indicates a potential galaxy cluster near a third candidate, with elliptical galaxies located at $z = 0.28$. The incidence of matches with known dusty galaxies and a potential lens candidate lends confidence to the selection of these DSFG candidates, even in the absence of strong 218 GHz detections.

There are eight DSFGs with $\alpha_{218-277} < 0$. Of these, six are nearby dusty galaxies. One, ACT-S J210551-001242, is a star that is a known radio source. As discussed above, CO contamination would enhance the flux densities in the 218 GHz band relative to the 277 GHz band. Also, if the galaxies are partially resolved such that some of the 277 GHz emission falls outside the beam, that could suppress the 277 GHz flux density relative to the 218 GHz flux density. In any case, all but one of these are confirmed to be dusty galaxies.

ORCID iDs

Megan B. Gralla  <https://orcid.org/0000-0001-9032-1585>
 Tobias A. Marriage  <https://orcid.org/0000-0003-4496-6520>
 Graeme Addison  <https://orcid.org/0000-0002-2147-2248>
 Andrew J. Baker  <https://orcid.org/0000-0002-7892-396X>
 Devin Crichton  <https://orcid.org/0000-0003-1204-3035>
 Mark Halpern  <https://orcid.org/0000-0002-1760-0868>
 Matt Hilton  <https://orcid.org/0000-0002-8490-8117>
 Kevin M. Huffenberger  <https://orcid.org/0000-0001-7109-0099>
 John P. Hughes  <https://orcid.org/0000-0002-8816-6800>
 Lyman A. Page  <https://orcid.org/0000-0002-9828-3525>
 Jesus Rivera  <https://orcid.org/0000-0003-3191-5193>
 Suzanne Staggs  <https://orcid.org/0000-0002-7020-7301>
 Ting Su  <https://orcid.org/0000-0002-6470-829X>
 Edward J. Wollack  <https://orcid.org/0000-0002-7567-4451>

References

Abdo, A. A., Ackermann, M., Ajello, M., et al. 2010, *ApJ*, 722, 520
 Alam, S., Albareti, F. D., Allende Prieto, C., et al. 2015, *ApJS*, 219, 12
 Aller, M. F. 1999, in ASP Conf. Ser. 159, BL Lac Phenomenon, ed. L. O. Takalo & A. Sillanpää (San Francisco, CA: ASP), 31
 Asboth, V., Conley, A., Sayers, J., et al. 2016, *MNRAS*, 462, 1989
 Astropy Collaboration, Robitaille, T. P., Tollerud, E. J., et al. 2013, *A&A*, 558, A33
 Austermann, J. E., Aretxaga, I., Hughes, D. H., et al. 2009, *MNRAS*, 393, 1573
 Austermann, J. E., Dunlop, J. S., Perera, T. A., et al. 2010, *MNRAS*, 401, 160
 Barger, A. J., Cowie, L. L., Sanders, D. B., et al. 1998, *Natur*, 394, 248
 Becker, R. H., White, R. L., & Helfand, D. J. 1995, *ApJ*, 450, 559
 Bertoldi, F., Carilli, C., Aravena, M., et al. 2007, *ApJS*, 172, 132
 Béthermin, M., Daddi, E., Magdis, G., et al. 2012, *ApJL*, 757, L23

Béthermin, M., Dole, H., Lagache, G., Le Borgne, D., & Penin, A. 2011, *A&A*, 529, A4
 Blain, A. W., Smail, I., Ivison, R. J., Kneib, J.-P., & Frayer, D. T. 2002, *PhR*, 369, 111
 Blandford, R. D., & Königl, A. 1979, *ApJ*, 232, 34
 Buckley, D. A. H., Swart, G. P., & Meiring, J. G. 2006, *Proc. SPIE*, 6267, 62670Z
 Burbidge, G., & Hewitt, A. 1992, in Variability of Blazars, ed. E. Valtaoja & M. Valtonen (Cambridge: Cambridge Univ. Press), 4
 Burgarella, D., Buat, V., Gruppioni, C., et al. 2013, *A&A*, 554, A70
 Bussmann, R. S., Perez-Fournon, I., Amber, S., et al. 2013, *ApJ*, 779, 25
 Cai, Z.-Y., Lapi, A., Xia, J.-Q., et al. 2013, *ApJ*, 768, 21
 Cañameras, R., Nesvadba, N. P. H., Guery, D., et al. 2015, *A&A*, 581, A105
 Casey, C. M., Narayanan, D., & Cooray, A. 2014, *PhR*, 541, 45
 Chambers, K. C., Magnier, E. A., Metcalfe, N., et al. 2016, arXiv:1612.05560
 Chapman, S. C., Blain, A. W., Smail, I., & Ivison, R. J. 2005, *ApJ*, 622, 772
 Ciprini, S., Takalo, L. O., Tosti, G., et al. 2007, *A&A*, 467, 465
 Coppin, K., Chapin, E. L., Mortier, A. M. J., et al. 2006, *MNRAS*, 372, 1621
 Coppin, K., Halpern, M., Scott, D., Borys, C., & Chapman, S. 2005, *MNRAS*, 357, 1022
 Crawford, T. M., Switzer, E. R., Holzapfel, W. L., et al. 2010, *ApJ*, 718, 513
 Daddi, E., Dickinson, M., Morrison, G., et al. 2007, *ApJ*, 670, 156
 Das, S., Louis, T., Nolta, M. R., et al. 2014, *JCAP*, 4, 14
 Datta, R., Aiola, S., Choi, S. K., et al. 2019, *MNRAS*, 486, 5239
 de Zotti, G., Ricci, R., Mesa, D., et al. 2005, *A&A*, 431, 893
 Dunne, L., & Eales, S. A. 2001, *MNRAS*, 327, 697
 Dünner, R., Hasselfield, M., Marriage, T. A., et al. 2013, *ApJ*, 762, 10
 Elbaz, D., Daddi, E., Le Borgne, D., et al. 2007, *A&A*, 468, 33
 Fan, X.-L., Li, S. K., Liao, N. H., et al. 2018, *ApJ*, 856, 80
 Fowler, J. W., Niemack, M. D., Dicker, S. R., et al. 2007, *ApOpt*, 46, 3444
 Geach, J. E., Ivison, R. J., Dye, S., & Oteo, I. 2018, *ApJL*, 866, L12
 Geach, J. E., More, A., Verma, A., et al. 2015, *MNRAS*, 452, 502
 Geach, J. E., Dunlop, J. S., Halpern, M., et al. 2017, *MNRAS*, 465, 1789
 Gralla, M. B., Crichton, D., Marriage, T. A., et al. 2014, *MNRAS*, 445, 460
 Gralla, M. B., & Marriage, T. 2020, *ApJ*, 893, 103
 Greve, T. R., Vieira, J. D., Weiss, A., et al. 2012, *ApJ*, 756, 101
 Greve, T. R., Weiss, A., Walter, F., et al. 2010, *ApJ*, 719, 483
 Hajian, A., Acquaviva, V., Ade, P. A. R., et al. 2011, *ApJ*, 740, 86
 Harrington, K. C., Yun, M. S., Cybulski, R., et al. 2016, *MNRAS*, 458, 4383
 Hasselfield, M., Hilton, M., Marriage, T. A., et al. 2013a, *JCAP*, 7, 008
 Hasselfield, M., Moodley, K., Bond, J. R., et al. 2013b, *ApJS*, 209, 17
 Henderson, S. W., Allison, R., Austermann, J., et al. 2016, *JLTP*, 184, 772
 Hezaveh, Y. D., & Holder, G. P. 2011, *ApJ*, 734, 52
 Hezaveh, Y. D., Marrone, D. P., Fassnacht, C. D., et al. 2013, *ApJ*, 767, 132
 Hodge, J. A., Becker, R. H., White, R. L., Richards, G. T., & Zeimann, G. R. 2011, *AJ*, 142, 3
 Holland, W. S., Bintley, D., Chapin, E. L., et al. 2013, *MNRAS*, 430, 2513
 Hopkins, A. M., & Beacom, J. F. 2006, *ApJ*, 651, 142
 Hughes, D. H., Serjeant, S., Dunlop, J., et al. 1998, *Natur*, 394, 241
 Hughes, P. A., Aller, H. D., & Aller, M. F. 1992, *ApJ*, 396, 469
 Landsman, W. B. 1993, in ASP Conf. Ser. 52, Astronomical Data Analysis Software and Systems II, ed. R. J. Hanisch, R. J. V. Brissenden, & J. Barnes (San Francisco, CA: ASP), 246
 Laurent, G. T., Aguirre, J. E., Glenn, J., et al. 2005, *ApJ*, 623, 742
 Le Floch, E., Papovich, C., Dole, H., et al. 2005, *ApJ*, 632, 169
 Lilly, S. J., Le Fevre, O., Hammer, F., & Crampton, D. 1996, *ApJL*, 460, L1
 Lindner, R. R., Baker, A. J., Omont, A., et al. 2011, *ApJ*, 737, 83
 Louis, T., Addison, G. E., Hasselfield, H., et al. 2014, *JCAP*, 7, 016
 Madau, P., & Dickinson, M. 2014, *ARA&A*, 52, 415
 Madau, P., Ferguson, H. C., Dickinson, M. E., et al. 1996, *MNRAS*, 283, 1388
 Magnelli, B., Lutz, D., Santini, P., et al. 2012, *A&A*, 539, A155
 Marriage, T. A., Baptiste, J., Lin, Y.-T., et al. 2011, *ApJ*, 731, 100
 Marsden, D., Gralla, M., Marriage, T. A., et al. 2014, *MNRAS*, 439, 1556
 McMahon, R. G., Banerji, M., Gonzalez, E., et al. 2013, *Msngr*, 154, 35
 Melin, J.-B., Bartlett, J. G., & Delabrouille, J. 2006, *A&A*, 459, 341
 Mocuano, L. M., Crawford, T. M., Vieira, J. D., et al. 2013, *ApJ*, 779, 61
 Murphy, T., Sadler, E. M., Ekers, R. D., et al. 2010, *MNRAS*, 402, 2403
 Nayyeri, H., Keele, M., Cooray, A., et al. 2016, *ApJ*, 823, 17
 Negrello, M., Hopwood, R., De Zotti, G., et al. 2010, *Sci*, 330, 800
 Negrello, M., Perrotta, F., González-Nuevo, J., et al. 2007, *MNRAS*, 377, 1557
 Nettek, W., Scott, D., Gibb, A. G., et al. 2017, *MNRAS*, 468, 250
 O'Riordan, M., Pe'er, A., & McKinney, J. C. 2017, *ApJ*, 843, 81
 Oliver, S. J., Bock, J., Altieri, B., et al. 2012, *MNRAS*, 424, 1614
 Page, L., Jackson, C., Barnes, C., et al. 2003, *ApJ*, 585, 566
 Papovich, C., Shipley, H. V., Mehrrens, N., et al. 2016, *ApJS*, 224, 28
 Pérez-González, P. G., Rieke, G. H., Egami, E., et al. 2005, *ApJ*, 630, 82

- Planck Collaboration, Ade, P. A. R., Aghanim, N., et al. 2011a, *A&A*, **536**, A13
- Planck Collaboration, Ade, P. A. R., Aghanim, N., et al. 2011b, *A&A*, **536**, A16
- Planck Collaboration, Ade, P. A. R., Aghanim, N., et al. 2011c, *A&A*, **536**, A7
- Planck Collaboration, Ade, P. A. R., Aghanim, N., et al. 2013, *A&A*, **550**, A133
- Planck Collaboration, Ade, P. A. R., Aghanim, N., et al. 2014, *A&A*, **571**, A28
- Planck Collaboration, Ade, P. A. R., Aghanim, N., et al. 2016, *A&A*, **594**, A26
- Rivera, J., Baker, A. J., Gallardo, P. A., et al. 2019, *ApJ*, **879**, 95
- Roberts-Borsani, G. W., Jimenez-Donaire, M. J., Dapra, M., et al. 2017, *ApJ*, **844**, 110
- Sievers, J. L., Hlozek, R. A., Nolta, M. R., et al. 2013, *JCAP*, **10**, 060
- Smail, I., Ivison, R. J., & Blain, A. W. 1997, *ApJL*, **490**, L5
- Spilker, J. S., Marrone, D. P., Aravena, M., et al. 2016, *ApJ*, **826**, 112
- Staguhn, J. G., Kovacs, A., Arendt, R. G., et al. 2014, *ApJ*, **790**, 77
- Strandet, M. L., Weiss, A., Vieira, J. D., et al. 2016, *ApJ*, **822**, 80
- Su, T., Marriage, T. A., Asboth, V., et al. 2017, *MNRAS*, **464**, 968
- Swetz, D. S., Ade, P. A. R., Amiri, M., et al. 2011, *ApJS*, **194**, 41
- Swinbank, A. M., Smail, I., Longmore, S., et al. 2010, *Natur*, **464**, 733
- Tegmark, M., & de Oliveira-Costa, A. 1998, *ApJL*, **500**, L83
- Thornton, R. J., Ade, P. A. R., Aiola, S., et al. 2016, *ApJS*, **227**, 21
- Timlin, J. D., Ross, N. P., Richards, G. T., et al. 2016, *ApJS*, **225**, 1
- Tingay, S. J., Jauncey, D. L., King, E. A., et al. 2003, *PASJ*, **55**, 351
- Toffolatti, L., Argueso Gomez, F., de Zotti, G., et al. 1998, *MNRAS*, **297**, 117
- Tucci, M., Toffolatti, L., de Zotti, G., & Martínez-González, E. 2011, *A&A*, **533**, A57
- Valiante, E., Smith, M. W. L., Eales, S., et al. 2016, *MNRAS*, **462**, 3146
- Vieira, J. D., Crawford, T. M., Switzer, E. R., et al. 2010, *ApJ*, **719**, 763
- Vieira, J. D., Marrone, D. P., Chapman, S. C., et al. 2013, *Natur*, **495**, 344
- Viero, M. P., Asboth, V., Roseboom, I. G., et al. 2014, *ApJS*, **210**, 22
- Vincent, M. B., Morse, J. A., Beland, S., et al. 2003, *Proc. SPIE*, **4841**, 367
- Wardlow, J. L., Cooray, A., De Bernardis, F., et al. 2013, *ApJ*, **762**, 59
- Weiß, A., De Breuck, C., Marrone, D. P., et al. 2013, *ApJ*, **767**, 88
- White, R. L., Becker, R. H., Helfand, D. J., & Gregg, M. D. 1997, *ApJ*, **475**, 479
- Wright, E. L., Eisenhardt, P. R. M., Mainzer, A. K., et al. 2010, *AJ*, **140**, 1868